

Chemo-mechanical model for degradation of oil paintings by amorphous and crystalline metal soaps

Citation for published version (APA):

Eumelen, G. J. A. M., Bosco, E., Suiker, A. S. J., & Hermans, J. J. (2023). Chemo-mechanical model for degradation of oil paintings by amorphous and crystalline metal soaps. *European Journal of Mechanics. A, Solids*, 97, Article 104827. <https://doi.org/10.1016/j.euromechsol.2022.104827>

Document license:
CC BY

DOI:
[10.1016/j.euromechsol.2022.104827](https://doi.org/10.1016/j.euromechsol.2022.104827)

Document status and date:
Published: 01/01/2023

Document Version:
Publisher's PDF, also known as Version of Record (includes final page, issue and volume numbers)

Please check the document version of this publication:

- A submitted manuscript is the version of the article upon submission and before peer-review. There can be important differences between the submitted version and the official published version of record. People interested in the research are advised to contact the author for the final version of the publication, or visit the DOI to the publisher's website.
- The final author version and the galley proof are versions of the publication after peer review.
- The final published version features the final layout of the paper including the volume, issue and page numbers.

[Link to publication](#)

General rights

Copyright and moral rights for the publications made accessible in the public portal are retained by the authors and/or other copyright owners and it is a condition of accessing publications that users recognise and abide by the legal requirements associated with these rights.

- Users may download and print one copy of any publication from the public portal for the purpose of private study or research.
- You may not further distribute the material or use it for any profit-making activity or commercial gain
- You may freely distribute the URL identifying the publication in the public portal.

If the publication is distributed under the terms of Article 25fa of the Dutch Copyright Act, indicated by the "Taverne" license above, please follow below link for the End User Agreement:

www.tue.nl/taverne

Take down policy

If you believe that this document breaches copyright please contact us at:

openaccess@tue.nl

providing details and we will investigate your claim.



Chemo-mechanical model for degradation of oil paintings by amorphous and crystalline metal soaps

G.J.A.M. Eumelen^a, E. Bosco^{a,*}, A.S.J. Suiker^a, J.J. Hermans^{b,c}

^a Department of the Built Environment, Eindhoven University of Technology, P.O. Box 513, 5600 MB Eindhoven, The Netherlands

^b Van 't Hoff Institute for Molecular Sciences, University of Amsterdam, P.O. Box 94720, 1090 GD Amsterdam, The Netherlands

^c Rijksmuseum Amsterdam, Conservation and Science, P.O. Box 7488, 1070 DN Amsterdam, The Netherlands

ARTICLE INFO

Keywords:

Multi-physics modelling
Discrete fracture
Historical paintings
Art conservation
Chemo-mechanical degradation

ABSTRACT

Metal soap formation is recognised as a critical degradation mechanism in historical oil paintings, which threatens the preservation of museum collections worldwide. Metal soaps form via a complex sequence of chemical reactions between metal ions released by the pigments and saturated fatty acids originating from the drying oil. The latest advances in chemistry research suggest that metal ions and saturated fatty acids may initially react by means of a reversible reaction, which leads to the formation of metal soaps in an amorphous state. Metal soaps may subsequently crystallise via an irreversible reaction into large aggregates that deform the paint layers, potentially triggering delamination, cracking, and ultimately flaking of the paint. This paper proposes a chemo-mechanical model to predict metal soap formation and the consequent mechanical damage in historical oil paintings. The chemical process is described in terms of a set of diffusion–reaction equations, which account for *both* the reversible reaction between free saturated fatty acids and metal ions forming amorphous metal soap, and the subsequent irreversible reaction to crystalline metal soap. The chemical model is two-way coupled with a mechanical model that effectively describes the cracking processes caused by metal soap formation and growth. The coupling is generated from the mechanical model by accounting for the development of a chemically-induced growth strain in the crystalline metal soap. In addition, the presence of cracks locally hampers the diffusion of chemical species, which is taken into account in the chemical model through a dependency of the diffusion parameter at the crack faces on the amount of mechanical damage generated. The spatial development of the crystalline metal soap phase is simulated by using a tailor-made scanning algorithm that identifies the reaction zone in which metal soap formation takes place. The proposed model is calibrated on experimental data presented in the literature. The model is subsequently applied to analyse two numerical examples that are representative of typical metal soap-related degradation processes observed in historical oil paintings, revealing that the growth process of crystalline metal soap, the deformation of the paint surface, and the consequent cracking and delamination patterns are predicted in a realistic fashion.

1. Introduction

The process of metal soap formation and growth has been identified by cultural heritage conservators as one of the most crucial degradation mechanisms for the appearance, integrity and longevity of historic oil paintings (Cotte et al., 2017; Noble, 2019). Metal soaps typically appear as opalescent aggregates that deform the pictorial layers, possibly protruding through the paint surface (Higgitt et al., 2003; Noble and Boon, 2007; Cotte et al., 2007; Keune and Boon, 2007). They may additionally lead to an increased transparency of the paint, thereby revealing the colour of the underlying paint layers (Noble and Boon, 2007). Metal soaps do not only influence the visual appearance of oil paintings, but may also promote cracking, delamination and ultimately

flaking of the paint (Maines et al., 2011; Helwig et al., 2014; Raven et al., 2019). Two striking examples of metal soap-induced degradation phenomena can be observed in Fig. 1. Fig. 1(a) illustrates a ceiling painting located in the Room of Trustees of the Burgerweeshuis in Zierikzee, The Netherlands, in which multiple metal soap crystals have formed inside the orange-red bottom paint film, causing a substantial deformation of the above pictorial layers. Fig. 1(b) represents *View of Delft* by Johannes Vermeer (Mauritshuis, The Hague, The Netherlands), in which a distinguishable, large metal soap aggregate has protruded through several paint layers and has reached the paint surface.

Metal soap formation and growth are governed by a complex sequence of chemical reactions, as schematically depicted in Fig. 2.

* Corresponding author.

E-mail address: e.bosco@tue.nl (E. Bosco).

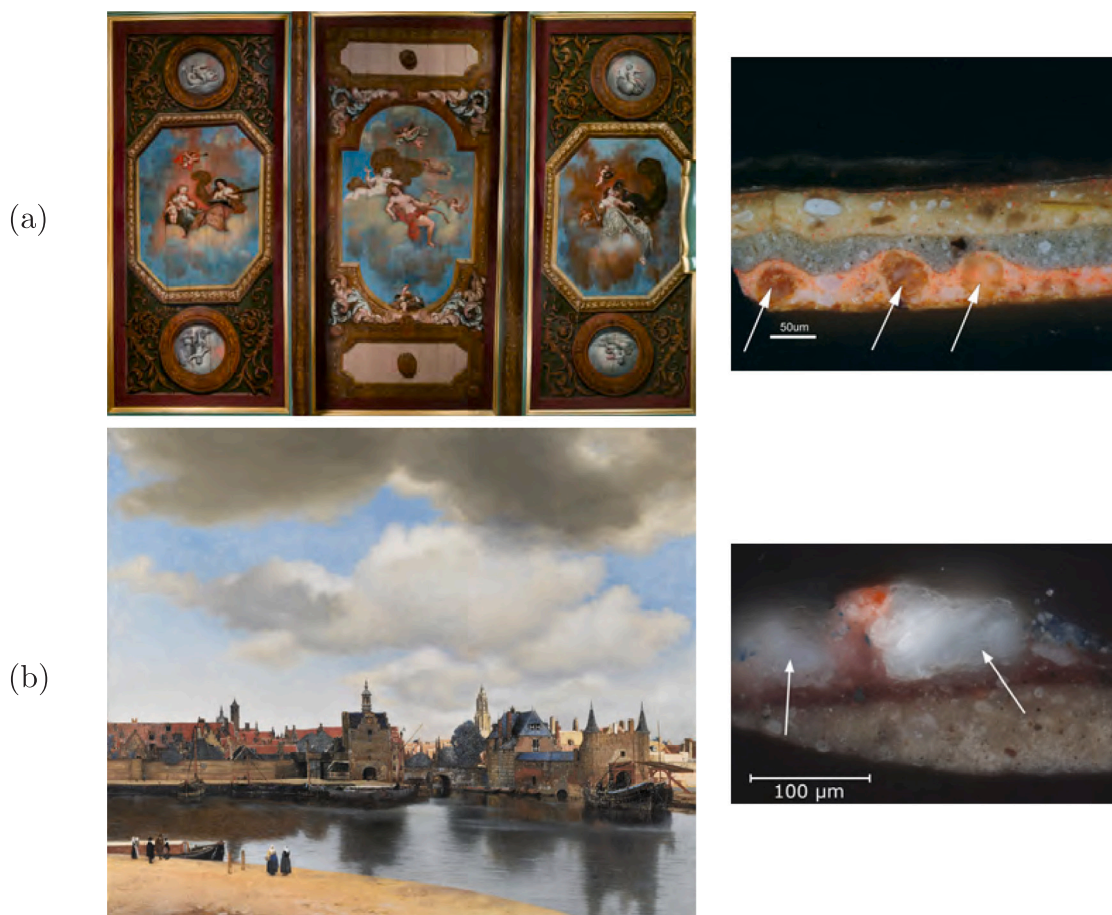


Fig. 1. Examples of metal soap-induced degradation mechanisms. (a) *Ceiling painting with allegorical representations*, 1680, Room of Trustees, Burgerweeshuis, Zierikzee, The Netherlands (Photo: Wim Ruijgaard). The detail shows a dark-field image of a sample cross-section taken from the red sky of Justitia and Mars in a Warm Embrace, right painting. In the bottom orange-red paint layer, which contains lead white and red lead, three lead soap protrusions have formed. An interface undulation can be observed in this cross-section, whereby the crystals in the bottom layer start to penetrate the layers above (Thoury et al., 2019). (b) Johannes Vermeer, *View of Delft*, ca. 1660–1661, Oil on canvas, Mauritshuis, The Hague, The Netherlands. The detail shows a bright-field image of a paint cross-section taken at the left edge of the painting, where the green (now blue) bush is painted over the red-tiled roof, showing the formation of large metal soap protrusions in the dark-red paint layer that have erupted through the blue-green surface paint layer (van Loon, 2009; van Loon et al., 2012). (For interpretation of the references to colour in this figure legend, the reader is referred to the web version of this article.)

Oil paintings consist of layers of a drying oil binding medium (typically linseed oil), which contain pigment particles and adhere to a substrate made of prepared canvas or wood. From a chemical point of view, drying oils are triglycerides, composed of three fatty acid molecules bound to a glycerol backbone via an ester bond. Fatty acids are carboxylic acids, i.e., organic compounds of carbon, oxygen and hydrogen, with long hydrocarbon chains (Lazzari and Chiantore, 1999). Most of the fatty acids chains in a drying oil are *unsaturated*, containing one or more C=C bonds. However, *saturated* fatty acids, such as palmitic and stearic acids, are also present in the oil binder, representing approximately 5%–15% of the total fatty acid content. During paint drying, the unsaturated fatty acid chains in the oil binder react by means of autoxidation reactions to form a densely cross-linked polymer network (van Gorkum and Bouwman, 2005; Baij et al., 2019; Bonaduce et al., 2019). Moreover, on a larger time scale, due to the presence of water molecules in the paint film, the ester bonds between the fatty acid chains and the glycerol backbone can be broken by means of hydrolysis reactions (Baij et al., 2019; van den Berg et al., 2001; van den Berg, 2002; Bonaduce et al., 2012). This leads to the release of free saturated fatty acids as a reaction product (Erhard et al., 2005). The process of metal soap formation is especially relevant in the case of lead- or zinc-based pigments, which are present, for instance, in the common lead white and zinc white paints (Keune et al., 2008). Lead and zinc ions that are released from the pigments may become complexed with the carboxyl groups (COOH) of the polymer

network, forming an ionomer (Hermans et al., 2015, 2016a; Baij et al., 2018a; Beerse et al., 2020), see Fig. 2(a). The free saturated fatty acids present in the system may further react with the metal ions from the ionomer, forming complexes of amorphous metal soaps, see Fig. 2(b). The formation of amorphous metal soaps is expected to be a reversible process, for which the metal ions can be bound either to the carboxylic acid groups of the ionomer or to those of the free saturated fatty acids (Hermans et al., 2015). If the local concentration of amorphous metal soap becomes sufficiently high, it can subsequently crystallise by means of an irreversible chemical reaction and coalesce into larger metal soap aggregates, reaching diameters varying between 50 and 500 μm (Noble and Boon, 2007), see Fig. 2(c).

Fig. 3 shows the internal material structure of a metal (zinc) soap nucleus at the nano-scale. The image, which has been taken from Hermans et al. (2018), has been obtained by using transmission electron microscopy, and clearly illustrates that the crystalline metal soap dendrites (indicated in red) that have developed inside the nucleus are surrounded by paint material (indicated in blue) based on a linseed oil polymer. In other words, the metal soap nuclei, and also the larger aggregates developing from these nuclei, are not fully occupied by crystalline metal soap, but also contain paint material, as confirmed from other experimental studies (Henderson et al., 2019; Ortiz Miranda et al., 2020). For simplicity reasons, however, in the present work the metal soap nuclei and aggregates will be designated as “metal soap crystals”, and in the model formulation are effectively treated

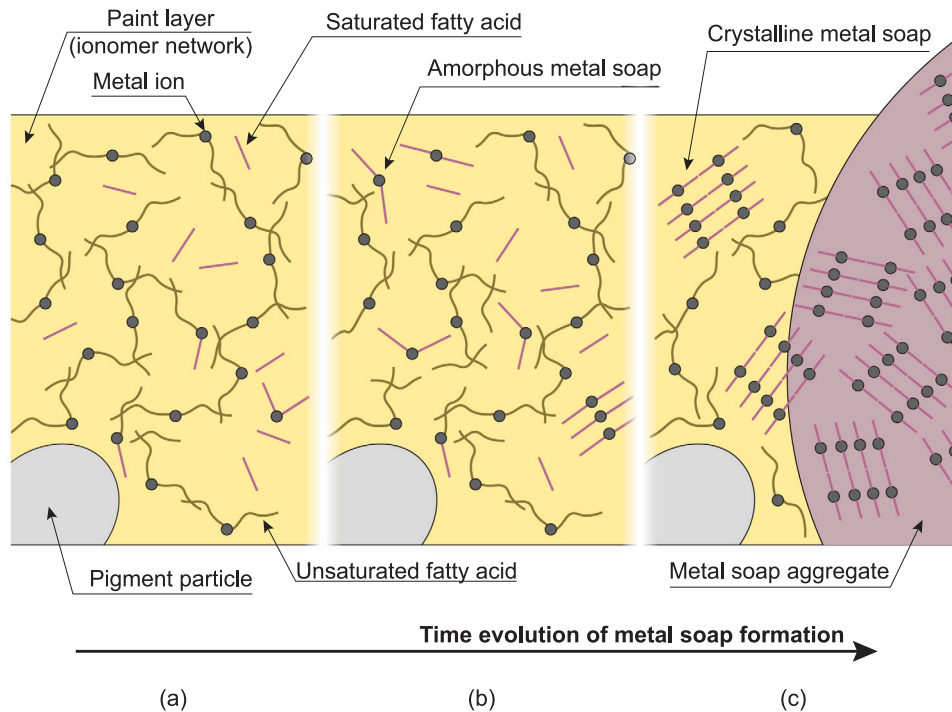


Fig. 2. Schematic representation of the processes governing metal soap formation. (a) During the drying process of the paint film, the oil binder polymerises into a densely cross-linked polymer network by means of autoxidation reactions and releases free saturated fatty acids as a degradation product. Metal ions, which are released from the pigment particles, become complexed with the polymer network, thereby forming an ionomer. (b) Metal ions from the ionomer react by means of a *reversible reaction* with the free saturated fatty acid molecules to form amorphous metal soap. (c) Amorphous metal soap crystallises by means of an *irreversible reaction* and grows in large metal soap aggregates.

as homogeneous and isotropic. The latter assumption is reasonable, as the model refers to the length scale associated to the thickness of a paint layer, i.e., the micro-scale, which is considerably larger than the nano-scale considered in Fig. 3. Nevertheless, in the numerical simulations the initial concentration of metal ions will be determined by considering that the aggregates are not fully occupied by crystalline metal soap, which essentially means that only a certain fraction of the metal ions present in the initial paint material is available for metal soap formation.

The process of metal soap formation has been primarily investigated in the literature from a chemical perspective, by focusing on the *in-situ* identification of metal soap in historic paintings (Noble et al., 2002; van der Weerd et al., 2002; Plater et al., 2003; Keune et al., 2011; Chen-Wiegart et al., 2017), or by exploring the kinetics of the chemical reaction (Cotte et al., 2006; MacDonald et al., 2016; Izzo et al., 2021) and the composition of metal soap aggregates (Hermans et al., 2016b). On the contrary, only a few studies are available that investigate the consequences of metal soap formation on the mechanical response of paint films. In van den Berg (2002), it has been reported that metal soap formation can contribute to an increase of oil paint stiffness and brittleness. Moreover, the presence of metal soap aggregates has been associated to micro-cracks and delamination phenomena (Maines et al., 2011; Helwig et al., 2014; Raven et al., 2019; Osmond et al., 2012), which are triggered by the mechanical strain (and thus stress) generated in the painting system under metal soap growth. Recently, a computational chemo-mechanical model has been proposed that predicts damage development in paint layers as a result of metal soap formation and growth (Eumelen et al., 2019). The model departs from a simplified chemical description in which the intermediate state of amorphous metal soap is neglected and *only* the irreversible crystallisation process is modelled. Accordingly, the diffusion-reaction model is formulated solely in terms of the concentration of saturated fatty acid and the volume fraction of crystalline metal soap formed. The chemo-mechanical model is implemented within a finite element

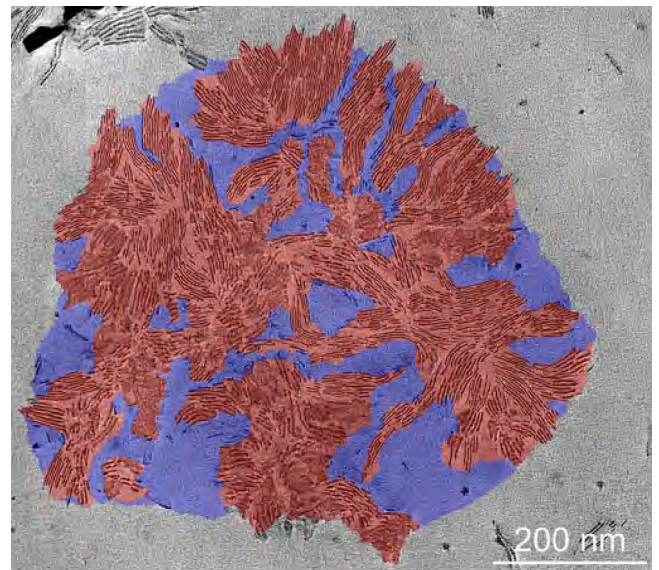


Fig. 3. Transmission electron microscope (TEM) bright field image of a metal soap nucleus, which contains crystalline zinc soap dendrites (indicated in red) that are surrounded by paint material (indicated in blue) based on a linseed oil polymer. The picture (without the colours) is taken from Hermans et al. (2018). (For interpretation of the references to colour in this figure legend, the reader is referred to the web version of this article.)

framework, whereby the chemical and mechanical fields are solved in an incremental-iterative fashion, using a staggered solution scheme.

Departing from the formulation presented in our previous work (Eumelen et al., 2019), in the present contribution the chemo-mechanical model for metal soap formation is substantially enhanced by accounting for *both* the reversible reaction between free saturated fatty acids and

metal ions forming amorphous metal soap, and the irreversible reaction governing the process of metal soap crystallisation. Along similar lines as the one-dimensional formulation proposed in Hermans (2017), these chemical processes are described via a set of (diffusion-)reaction equations in terms of the concentrations of free saturated fatty acids, metal ions, amorphous metal soap and crystalline metal soap. Although, in principle, both the free saturated fatty acids and the metal ions can diffuse in the ionomer (Tudry et al., 2012), metal ion diffusion is ignored here, as this process typically is very slow compared to fatty acid diffusion. As a consequence, the free saturated fatty acids are considered as the sole diffusing species, for which a diffusion–reaction equation is formulated, whereas the time evolution of the concentrations of the metal ions and the amorphous and crystalline metal soaps are governed by reaction equations. Along the lines of Eumelen et al. (2019), the coupling between the diffusion–reaction model and the mechanical analysis is obtained by defining a chemically-induced growth strain, which quantifies the effect of the expansion of the growing metal soap crystal on the stress field generated in the painting. Additionally, the local change in the mechanical properties associated to the formation of crystalline metal soap is computed by a basic phase transformation model, whereby the effective stiffness is obtained as the volume average of the properties of the material phases present in the specific material point. Mechanical equilibrium equations finally complete the definition of the mechanical problem. The paint geometry is discretised into plane-strain continuum elements that represent the two-dimensional bulk responses of the metal soap and paint materials. Further, in order to describe the onset and propagation of discrete cracks at arbitrary locations in the paint domain, cohesive interface elements are placed between all continuum elements modelling the paint configuration, in correspondence with the approach originally proposed in Xu and Needleman (1994). The constitutive behaviour of a crack is defined in accordance with the interface damage model proposed in Cid Alfaro et al. (2009). The presence of cracks locally hampers the diffusion of the free saturated fatty acids, which is accounted for by specifying the constitutive relation between the flux and the concentration of free saturated fatty acids across a crack as a function of the mechanical damage. Consequently, the chemo-mechanical model is two-way coupled.

The enhanced chemo-mechanical model proposed in this work is applied to analyse two different boundary value problems, which are representative of typical metal soap-related degradation mechanisms observed in historical paintings. The first boundary value problem focuses on the interplay between the growth process and coalescence of *multiple metal soap crystals* and the crack patterns generated in a *single-layer paint system*. The second boundary value problem refers to a *multi-layer paint system* composed of an upper pictorial layer and a supporting ground layer, and focuses on the competition between surface cracking in the upper layer and delamination at the interface between the two layers, as induced by the formation and growth of a *single metal soap crystal* in the ground layer.

This paper is organised as follows. Section 2 describes the chemo-mechanical modelling framework, including the diffusion–reaction equations, the mechanical model and the coupling terms between the two physical processes. In Section 3, the chemical properties that serve as input for the diffusion–reaction model are calibrated based on the experimental results presented in Hermans (2017). Section 4 treats the definition of the geometry, material properties, initial and boundary conditions and the numerical results of the *single-layer paint model*. In Section 5, the geometrical details, input parameters, initial and boundary conditions and simulation results of the *multi-layer paint model* are discussed. Finally, the main conclusions of the work are summarised in Section 6.

2. Model description

The chemo-mechanical model describing the degradation of oil paintings by metal soap formation consists of a chemical model and a mechanical model, which are successively described in Sections 2.1 and 2.2. The numerical solution procedure that is used to solve the coupled chemical and mechanical models is reviewed in Section 2.3.

2.1. Chemical model

Departing from the formulation presented in Eumelen et al. (2019), in the present contribution the chemo-mechanical model for metal soap formation is substantially enhanced by accounting for *both* the reversible reaction forming amorphous metal soap, and the irreversible reaction leading to metal soap crystallisation. The proposed model is based on the following assumptions. First, the initial state of the domain is assumed to be represented by an ionomer characterised by given concentrations of free saturated fatty acids and metal ions. Accordingly, the autoxidation reactions leading to the formation of the ionomer and the reactions associated to the release of free saturated fatty acids by the oil binder and the metal ions from the pigments are not explicitly modelled. Moreover, despite that the paint is a heterogeneous material, composed of the ionomer with embedded pigment particles, it is here treated as an equivalent, homogeneous continuum, characterised by effective chemical and mechanical properties. The paint and the fully crystallised metal soap are the two physical material phases that together form the paint system. Conversely, the free saturated fatty acids, the metal ions, and the amorphous metal soaps only enter the model through their concentrations. It is assumed that metal soap crystallisation develops from pre-existing crystal nuclei, which are small regions in which fully crystallised metal soap is present, see Fig. 3. The chemical reactions leading to metal soap formation are enforced to occur in a (moving) transition region named the “reaction zone”, which is located at the interface between the metal soap crystal and the adjacent paint material.

The chemical process leading to the formation of crystalline metal soap can be expressed by means of two successive chemical reactions (Hermans, 2017):



in which $M + nFa$ denotes a metal ion M reacting with n free saturated fatty acid molecules Fa . The term MFa_n indicates the metal soap complex, for which prefixes “a” and “c” refer to the amorphous and crystalline states of the metal soap compound, respectively. Further, k_+ and k_- are the rate constants for the formation and dissolution of amorphous metal soap, respectively, while k_{crys} is the rate constant of the irreversible crystallisation reaction. In the present work lead-based pigments will be considered, for which $n = 2$. The chemical reactions described by Eq. (1) can be converted to a system of diffusion–reaction equations, expressed in terms of the individual species that are involved in the chemical process, i.e., saturated fatty acids, metal ions, amorphous and crystalline metal soaps. However, the diffusion process of saturated fatty acids is characterised by a significantly smaller characteristic time scale than that of the metal ions (Baij et al., 2018a) and of the amorphous or crystalline metal soap compounds. Hence, metal ion diffusion and amorphous metal soap diffusion are ignored, and the free saturated fatty acids are selected as the sole diffusing species.

Based on the above assumptions, the chemical process is defined by the following system of coupled (diffusion-)reaction equations (Hermans, 2017):

$$\begin{cases} \frac{\partial[M]}{\partial t} = -Q_{\text{aMFA}_2}, \\ \frac{\partial[\text{aMFA}_2]}{\partial t} = Q_{\text{aMFA}_2} - Q_{\text{cMFA}_2}, \\ \frac{\partial[\text{cMFA}_2]}{\partial t} = Q_{\text{cMFA}_2}, \\ \frac{\partial[\text{Fa}]}{\partial t} - \nabla \cdot (D\nabla[\text{Fa}]) = -2Q_{\text{aMFA}_2}. \end{cases} \quad (2)$$

Here $[i]$, with $[i] \geq 0$, represents the available concentration of the chemical species i , with $i = \text{Fa}$, M , aMFA_2 and cMFA_2 . Further, t represents time, and $\nabla \cdot$ denotes the divergence operator, with ∇ being the gradient operator. Finally, D indicates the diffusion coefficient.

Refer first to Eqs. (2)₁–(2)₃ that describe the development of the concentration of the species $i = \text{M}$, aMFA_2 and cMFA_2 that react but do not diffuse. The minus sign in front of some of the reaction terms Q_i indicates that, if the value of Q_i is positive, the corresponding species i is consumed during the specific chemical reaction. Define now \mathcal{R}_i^+ as the reaction rate of the reactants, which characterises the “forward reaction”, and \mathcal{R}_i^- as the reaction rate of the reaction products, characterising the “backward reaction”. Following Oxtoby et al. (2008), the reaction terms Q_{aMFA_2} and Q_{cMFA_2} can be expressed as

$$\begin{aligned} Q_{\text{aMFA}_2} &= \mathcal{R}_{\text{aMFA}_2}^+ - \mathcal{R}_{\text{aMFA}_2}^-, \\ Q_{\text{cMFA}_2} &= \mathcal{R}_{\text{cMFA}_2}^+. \end{aligned} \quad (3)$$

Note that Eq. (1)₂ describes the irreversible chemical reaction from amorphous towards crystalline metal soap. Therefore, in Eq. (3)₂, the reaction term Q_{cMFA_2} is prescribed to be non-negative, $Q_{\text{cMFA}_2} \geq 0$. The specific expressions for the forward and backward reaction rates in Eqs. (3) can be formulated in terms of the concentrations of the involved species, raised to a power equal to their stoichiometric coefficient (Oxtoby et al., 2008; Zumdahl and Zumdahl, 2017). Considering the chemical reactions, Eq. (1), and recalling again that $n = 2$, leads to

$$\begin{aligned} \mathcal{R}_{\text{aMFA}_2}^+ &= k_+[M][\text{Fa}]^2, \\ \mathcal{R}_{\text{aMFA}_2}^- &= k_-[\text{aMFA}_2], \\ \mathcal{R}_{\text{cMFA}_2}^+ &= k_{\text{crys}}[\text{aMFA}_2]. \end{aligned} \quad (4)$$

Inserting Eqs. (4) into Eqs. (3) finally specifies the reaction terms Q_{aMFA_2} and Q_{cMFA_2} as

$$\begin{aligned} Q_{\text{aMFA}_2} &= k_+[M][\text{Fa}]^2 - k_-[\text{aMFA}_2], \\ Q_{\text{cMFA}_2} &= k_{\text{crys}}[\text{aMFA}_2], \end{aligned} \quad (5)$$

which need to be substituted in the system of (diffusion-)reaction equations, Eq. (2).

Consider now Eq. (2)₄ that describes the diffusion and reaction processes of the free saturated fatty acids $[\text{Fa}]$. The reaction term Q_{aMFA_2} present in the right-hand side of the equation is defined by Expression (5)₁, and introduces a coupling with the reaction equations, Eqs. (2)₁–(2)₃, of the non-diffusing species. Note further that the factor of 2 appearing in front of the reaction term Q_{aMFA_2} in Eq. (2)₄ accounts for the conservation of mass and equals the stoichiometric coefficient $n = 2$ of fatty acids $[\text{Fa}]$ in the corresponding chemical reaction, Eq. (1)₁. Further, in accordance with the experimental observations presented in Hermans (2017), the diffusion coefficient D is assumed to vary between the diffusion coefficients of the two physical material phases, i.e., the paint without any metal soap and the fully crystallised metal soap. This variation is quantified by the local volume fraction of the crystalline metal soap ϕ as

$$D = \phi D_s + (1 - \phi)^b D_p \quad \text{with} \quad 0 \leq \phi \leq 1, \quad (6)$$

where D_p and D_s are the diffusion coefficients for fatty acid diffusion in the paint and in the crystalline metal soap, with the subscripts

“p” and “s” referring to “paint” and “soap”, respectively. Further, the exponent $b \geq 1$ is a constant that determines the rate at which the diffusion coefficient decreases as a function of the volume fraction ϕ of crystalline metal soap formed. The value of ϕ is determined by the ratio between the current concentration $[\text{cMFA}_2]$ and the maximum concentration $[\text{cMFA}_2]_{\text{max}}$ of crystalline metal soap, i.e.,

$$\phi = \frac{[\text{cMFA}_2]}{[\text{cMFA}_2]_{\text{max}}}. \quad (7)$$

The maximum concentration of crystalline metal soap $[\text{cMFA}_2]_{\text{max}}$ is dictated by the initial concentration of metal ions $[\text{M}](t = 0) = [\text{M}]_0$, which, in accordance with the reaction equations given by Eq. (1), drives the formation of amorphous and crystalline metal soaps. Based on the reaction equations, Eq. (1), and considering that metal ions and metal soaps do not diffuse, from the conservation of mass the maximum concentration of crystalline metal soap can be computed as $[\text{cMFA}_2]_{\text{max}} = [\text{M}]_0$.

Eqs. (2), to be completed with appropriate initial and boundary conditions, describe the concentration development of the metal ions, amorphous and crystalline metal soaps and free saturated fatty acids in the painting. According to these equations, metal soap formation can in principle occur at any location in the domain where free saturated fatty acids are present, provided that $\phi \neq 1$. As discussed above, the metal soap growth process is assumed to depart from a crystalline nucleus of a small, specified size, for which $\phi = 1$. The chemical reactions are allowed to occur only in a small transition region located in between the metal soap crystal and the adjacent paint material, termed the *reaction zone*. Within this reaction zone, the volume fraction of crystalline metal soap is characterised by $0 < \phi < 1$, and the evolution of all chemical species is governed by the full system of (diffusion-)reaction equations, Eq. (2). The reaction zone is defined via a scanning algorithm that identifies the uncrystallised material points present within a small, prescribed radial distance from the crystallised material points located closest to the current boundary of the metal soap crystal, see Eumelen et al. (2019) for more background information on the scanning algorithm. In the remaining domain, where either $\phi = 0$ (paint) or $\phi = 1$ (crystalline metal soap), the reaction term Q_{cMFA_2} is set to 0 and the diffusion coefficient is specified, respectively, as D_p (paint) or D_s (crystalline metal soap).

2.2. Mechanical model

2.2.1. Continuum model

The mechanical model applied in this work is based on the formulation presented in Eumelen et al. (2019), as reviewed below. In any material point of the domain, the total strain tensor ϵ is defined as the sum of the elastic strain tensor ϵ^c and a growth strain tensor ϵ^g :

$$\epsilon = \epsilon^c + \epsilon^g. \quad (8)$$

The growth strain tensor ϵ^g describes the volumetric expansion of the metal soap during the crystallisation process (Noble and Boon, 2007; Keune and Boon, 2007; Boon et al., 2003) and is taken to be proportional to the volume fraction ϕ of crystalline metal soap (Eumelen et al., 2019):

$$\epsilon^g = \phi \epsilon^g \mathbf{I} \quad \text{with} \quad 0 \leq \phi \leq 1, \quad (9)$$

where ϕ is defined in accordance with Eq. (7), ϵ^g is the growth strain associated to the formation of crystalline metal soap, and \mathbf{I} is the second-order identity tensor. The formation and growth of crystalline metal soap thus induces stresses and strains in the paint layer, thereby generating a coupling between the chemical and mechanical fields. For material points in the paint phase ($\phi = 0$), the growth strain is equal to zero, and the total strain reduces to the elastic strain:

$$\epsilon_p = \epsilon_p^c. \quad (10)$$

Conversely, in material points located in the fully crystallised metal soap phase ($\phi = 1$), the growth strain reaches its maximum value $\epsilon_s^g = \epsilon^g I$, whereby the total strain is expressed by

$$\epsilon_s = \epsilon_s^e + \epsilon_s^g. \quad (11)$$

Finally, for material points in the reaction zone, where the paint and the metal soap phases are jointly present ($0 < \phi < 1$), Eq. (8) specifies into:

$$\epsilon_{rz} = \epsilon_{rz}^e + \epsilon_{rz}^g \quad \text{with} \quad \epsilon_{rz}^g = \phi \epsilon^g I \quad (12)$$

where the subscript rz refers to “reaction zone”.

Departing from the above description, a constitutive assumption needs to be made for the two material phases considered, i.e., the paint and the crystalline metal soap. In general, the mechanical properties of oil paints depend on the type of pigment particles, drying oils and pigment to binder volume ratio, as well as the age of the paint and the specific environmental conditions, see Mecklenburg et al. (2004, 2012), Fuster-López et al. (2016), Hagan (2017), Fuster-López et al. (2019). In the present work, the “bulk behaviour” of the paint and the crystalline metal soap, for simplicity, is considered to be isotropic linear elastic, in accordance with the expressions

$$\sigma_p = {}^4C_p : \epsilon_p^e \quad \text{and} \quad \sigma_s = {}^4C_s : \epsilon_s^e, \quad (13)$$

where 4C_p and 4C_s are the fourth-order elastic stiffness tensors of the paint and crystalline metal soap, respectively, and σ_p and σ_s are the corresponding stress tensors. Further, the symbol “:” denotes a double tensorial contraction. In order to describe the transformation from the paint material to the crystalline metal soap material, a basic phase transformation model is constructed as follows: Consider a material point located in the interfacial reaction zone, in which both the paint and the metal soap phases are present ($0 < \phi < 1$). Here, the total strain is assumed to be the same for both phases, $\epsilon_{rz} = \epsilon_s = \epsilon_p$, i.e., Voigt’s assumption is adopted, as a result of which the effective Cauchy stress tensor σ_{rz} follows from the weighted volume average of the stresses in the individual constituents (Eumelen et al., 2019; Hille et al., 2009):

$$\sigma_{rz} = \phi \sigma_s + (1 - \phi) \sigma_p \quad \text{with} \quad 0 < \phi < 1. \quad (14)$$

With the above constitutive models for the paint, crystalline metal soap, and their mixture in the reaction zone, Eqs. (13) and (14), in the absence of body forces the material response in any point of the domain is governed by the mechanical equilibrium equation

$$\nabla \cdot \sigma = 0. \quad (15)$$

Eq. (15) is completed by the appropriate boundary conditions.

2.2.2. Interface damage model

The stress field generated in a paint layer as a result of metal soap formation may trigger the onset and propagation of cracks. The discrete cracking behaviour of the paint is simulated by surrounding the continuum elements in the finite element model with interface elements equipped with a mixed-mode interface damage model. This modelling strategy was originally proposed in Xu and Needleman (1994), and allows for the robust simulation of crack patterns at arbitrary locations and in arbitrary directions. It naturally includes the effects of crack bifurcation, crack branching and crack coalescence, as previously demonstrated for applications related to historical paints (Eumelen et al., 2019, 2020, 2021), wood (Luimes et al., 2018; Schepboer et al., 2019; Luimes and Suiker, 2021), polymers (Tijssens et al., 2000), fibrous composites (Cid Alfaro et al., 2010a,b; Geng and Suiker, 2019) and cementitious materials (Schepboer et al., 2021). The interface elements are characterised by the interface damage model proposed in Cid Alfaro et al. (2009). The fracture process in a material point initiates when the effective interfacial traction attains the value of the ultimate fracture strength of the material t^u , which corresponds to a relative crack face separation v^u , as shown in Fig. 4. The fracture

process is defined by a linear softening branch, for which the tensile strength progressively decays as a function of a damage parameter d that can vary between 0 (no damage) and 1 (damage completion). The elastic interfacial stiffness consequently decreases as $(1 - d)K$. The evolution of the fracture process is monitored by a damage history variable κ . The fracture process is completed when the interfacial material point has lost its strength ($d = 1$), which occurs when the relative ultimate crack face separation v^u is reached. The toughness G_c is obtained as the area under the traction–separation law, with $G_c = t^u v^u / 2$. A damage loading function is defined that governs the loading and unloading conditions during fracture. The evolution of the fracture process is described by a rate-dependent kinetic law. The adopted model additionally accounts for the mode-mixity of the fracture process, by considering a combination of the crack face separations in the normal and tangential directions of the crack. This enables to distinguish between the contributions of mode I (tension) and mode II (shear) cracking. For more details on the interface damage model and its numerical implementation, the reader is referred to Cid Alfaro et al. (2009).

The presence of cracks in the domain has consequences for the chemo-diffusive response of the system, since, across the crack surfaces, the diffusion of the free saturated fatty acids is reduced. In order to account for this coupling effect, following Eumelen et al. (2019), Luimes and Suiker (2021), in the diffusion–reaction model the concentration of the free saturated fatty acids across a discrete crack is assumed to be discontinuous while the flux is taken as continuous. Denoting the concentration jump of free saturated fatty acids across a crack as $\llbracket \text{Fa} \rrbracket$, the corresponding flux is $J_{\text{Fa}} = \mathbf{j}_{\text{Fa}} \cdot \mathbf{n}$, where \mathbf{j}_{Fa} is the mass flux vector of the fatty acid species Fa, and \mathbf{n} is the unit vector normal to the crack faces. The flux–concentration relation is given by

$$J_{\text{Fa}} = D_c \llbracket \text{Fa} \rrbracket, \quad (16)$$

where D_c is the crack-reduced diffusion coefficient of the paint material, which is assumed to evolve as a function of the damage parameter d as

$$D_c = (1 - d) D_p. \quad (17)$$

2.3. Numerical solution procedure

The coupled chemo-mechanical analysis is performed with the aid of the commercial finite element package ABAQUS standard,¹ employing tailored user-subroutines for incorporating (i) the scanning algorithm described in Section 2.1 that is used for identifying and updating the interfacial reaction zone, (ii) the phase transformation model applied in the reaction zone, Eq. (14), (iii) the interface damage model employed for modelling discrete cracking, as outlined in Section 2.2.2, and (iv) the crack-reduced diffusion effect following from Eqs. (16) and (17). The chemical and mechanical field variables are solved for each time increment using a staggered, incremental-iterative update procedure, with the couplings between the chemical and mechanical fields established via a temporal extrapolation. The time increment is chosen relatively small, such that the error introduced by the time discretisation has a negligible influence on the numerical result. Each time increment starts with solving the coupled set of (diffusion-)reaction equations of the chemical model, as given by Eq. (2). The reactions between the various chemical species are hereby considered in the actual (updated) interfacial reaction zone between the paint material and the crystalline metal soap, which is constructed by applying the scanning algorithm described in Section 2.1. The flux of the free saturated fatty acids across crack surfaces is determined via Eq. (16), whereby the crack-reduced diffusion coefficient in the paint material is determined from Eq. (17) using the damage value d computed at

¹ Dassault Systems Simulia Corp, Providence, RI, U.S.A.

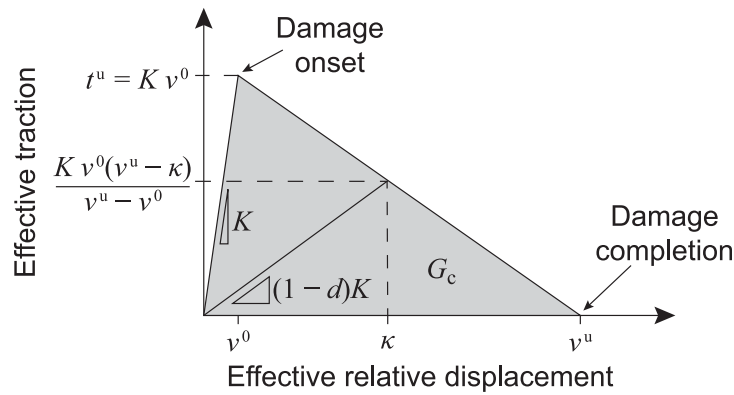


Fig. 4. Traction–separation law of the interface damage model.
Source: Taken from Cid Alfaro et al. (2009).

the previous time increment. The solution of the coupled diffusion–reaction, Eqs. (2), provides the concentration fields of all chemical species, i.e., the concentrations of the free saturated fatty acids [Fa], metal ions [M], amorphous metal soap [aMFa₂] and crystalline metal soap [cMFa₂]. With this result, the volume fraction of crystalline metal soap ϕ is updated via Eq. (7). The values of ϕ are next transferred to the mechanical analysis, where they are used for calculating the growth strain tensor ϵ^g in accordance with Eq. (9). Additionally, the stresses in the paint and crystalline metal soap are computed from Eq. (13), and the stresses inside the interfacial reaction zone are calculated as a function of ϕ via Eq. (14). With this result, the equilibrium Eqs. (15) governing the mechanical problem are solved in an iterative fashion, thereby accounting for the nucleation and propagation of discrete cracks in accordance with the interface damage model outlined in Section 2.2.2. The converged iterative procedure provides the updates of the overall displacement field and the damage parameter d in the integration points. The updated damage parameter d is subsequently transferred to the chemical analysis, after which the incremental-iterative solution procedure above is repeated for the next time increment.

3. Parameter calibration for the diffusion–reaction model

The material parameters for the chemical model described by Eqs. (2), (5) and (6), are calibrated from the experimental measurements reported in Hermans (2017), which are briefly reviewed in Section 3.1. The calibration procedure applied and the parameter values obtained are presented in Sections 3.2 and 3.3, respectively.

3.1. Review of the experiment

The experiments discussed in Hermans (2017) focus on measuring the time evolution of the concentration of crystalline metal soap forming from a lead-containing ionomer exposed to a fatty acid solution. An ionomer sample was prepared that consisted of a lead sorbate² mixed with cold-pressed linseed oil. Note that recent experimental works on similar model systems containing zinc sorbate have revealed that zinc sorbate samples exhibit mechanical properties, solvent diffusion behaviour and a molecular structure that are comparable to those of typical zinc white oil paint films (Hermans et al., 2019; Baij et al., 2018b). The employed lead sorbate model system can thus be considered as representative of real oil paint layers.

The prepared mixture of linseed oil and lead sorbate was next spread on a glass plate and cured overnight in an oven. The resulting ionomer film, which was characterised by an average thickness $l_s = 150 \mu\text{m}$,

was next placed at the bottom of an attenuated total reflection-Fourier transform infrared (ATR-FTIR) measurement cell. The measurement cell was subsequently filled with a solution of fatty acid (i.e., palmitic acid) and acetone over a height l_{Fa} that ranged between 10 mm and 20 mm, as schematically indicated in Fig. 5(a). In the designed experimental setup, a one-dimensional diffusion–reaction process is activated, whereby the fatty acid diffuses along the vertical direction in the fatty acid–acetone mixture. Furthermore, the fatty acid, together with acetone, diffuses in the ionomer sample below, whereby it reacts to form metal soap. The process of metal soap formation was monitored by measuring the concentration of crystalline metal soap formed at the bottom of the ionomer sample, using time-dependent ATR-FTIR measurements.

3.2. Reference model and calibration procedure

In order to identify the kinetic reaction constants and the diffusion coefficients associated to the diffusion and reaction of saturated fatty acids in the ionomer film, the experimental set-up indicated in Fig. 5(a) has been idealised to a one-dimensional model. In this model, which is shown in Fig. 5(b), the height of the saturated fatty acid solution and the thickness of the ionomer sample are represented by two adjacent segments of length l_{Fa} and l_s , respectively. The thickness of the ionomer sample equals $l_s = 150 \mu\text{m}$ (Hermans, 2017). The height of the palmitic acid–acetone solution has been taken equal to the lowest value considered in the experiments, $l_{\text{Fa}} = 10 \text{ mm}$. Note however, that a variation of this value in the range of 10 to 20 mm is expected to have a negligible effect on the experimental result, since the sample thickness l_s is much smaller than the height l_{Fa} of the saturated fatty acid solution, i.e., $l_s/l_{\text{Fa}} \ll 1$. This hypothesis has been confirmed by simulations not presented here.

In the experiment, the saturated fatty acids diffuse through the acetone solution, and further diffuse and react within the ionomer below, see Fig. 5(b). Accordingly, the one-dimensional diffusion process in the acetone solution can be described via the diffusion equation:

$$\frac{\partial[\text{Fa}]}{\partial t} - D_a \frac{\partial^2[\text{Fa}]}{\partial x^2} = 0, \quad (18)$$

where D_a is the diffusion coefficient of the saturated fatty acid in acetone, whereby the subscript “a” refers to the “hosting medium” (i.e., acetone). Further, for the ionomer sample it is assumed that the diffusion–reaction processes leading to metal soap formation are governed by the one-dimensional formulation of the system of chemical equations given by Eq. (2), complemented with the definitions in Eqs. (5), (6) and (7).

The boundary value problem described by the geometry presented in Fig. 5(b) and governed by Eqs. (18) (acetone solution) and (2) (ionomer sample) must be completed by initial and boundary conditions. In the measurement cell, the initial concentration of saturated

² A salt from sorbic acid.

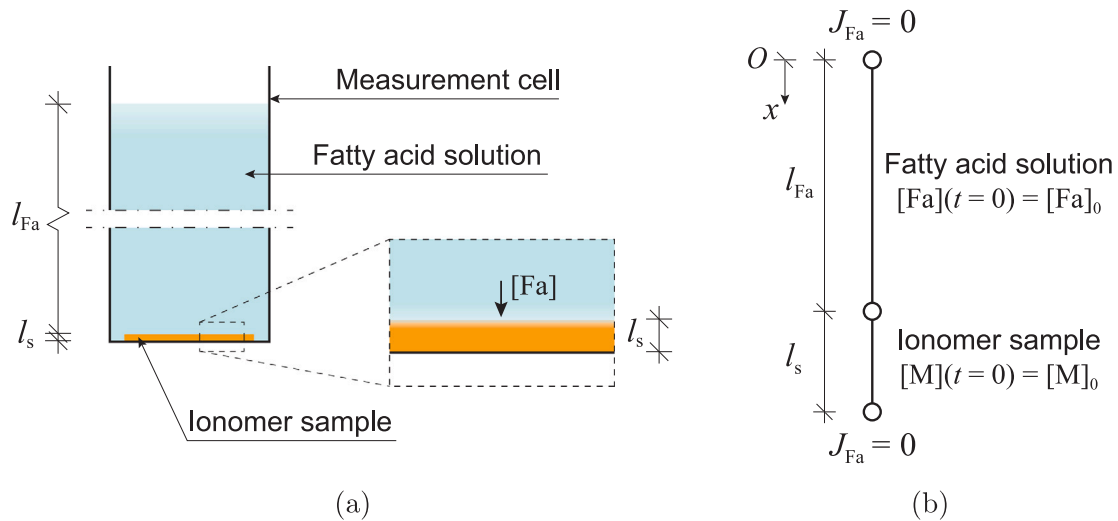


Fig. 5. (a) Schematic representation of the experiment reported in Hermans (2017). The experimental set-up consisted of a lead-based ionomer sample with a thickness l_s located at the bottom of an ATR-FTIR measurement cell, which was filled with a mixture of palmitic acid and acetone over a height l_{Fa} . The concentration of crystalline metal soap forming from the reaction of the palmitic acid with the lead ions from the ionomer was evaluated at the bottom of the ionomer by means of ATR-FTIR measurements. (b) One-dimensional schematisation of the experimental setup presented in Hermans (2017), with the corresponding initial and boundary conditions.

fatty acid is uniform and equal to $[Fa](t=0) = [Fa]_0 = 55 \text{ mol/m}^3$ (Hermans, 2017). In addition, zero-flux boundary conditions $J_{Fa} = 0$ are adopted at the external boundaries $x = 0$ and $x = l_{Fa} + l_s$, which reflect that no saturated fatty acids were added to the palmitic acid-acetone solution after the experiment had started, and that the saturated fatty acids could not diffuse outside the measurement cell. Furthermore, the initial metal ion concentration $[M](t=0) = [M]_0$ is taken as uniform within the ionomer sample and equals $[M]_0 = 160 \text{ mol/m}^3$ (Hermans, 2017).

Eqs. (2), (5), (6), (7) and (18) have been implemented in the mathematical software program MATLAB, and solved using the standard partial differential equation solver. The computational result has been subjected to a non-linear, least-squares fitting procedure, in order to match the concentration of crystalline metal soap $[cMFA_2]$ measured at the bottom of the sample, $x = l_{Fa} + l_s$, as reported in Hermans (2017). For this purpose, the diffusion coefficient of the saturated fatty acid in acetone has been selected as $D_a = 6.1 \cdot 10^{-11} \text{ m}^2/\text{s}$ (Hermans, 2017). Correspondingly, the calibrated parameters are the reaction rates k_+ , k_- and k_{crys} , the diffusion coefficients D_p and D_s , and the exponent b in Eq. (6) that governs the transition of the diffusion coefficient in the ionomer from D_p to D_s .

3.3. Result of calibration procedure

Fig. 6 shows the time evolution of the concentration of crystalline metal soap $[cMFA_2]$, evaluated at the bottom of the ionomer sample, as obtained from the experimental measurement (black line) and the numerical simulation (red line). From the solution of Eqs. (2) and (18), combined with the calibration procedure described above, the model parameters have been determined in correspondence with an R^2 -value of 0.9748. Accordingly, the kinetic reaction constants are obtained as $k_+ = 0.491 \cdot 10^{-6} \text{ m}^6 \cdot (\text{mol}^2 \text{ s})^{-1}$, $k_- = 0.169 \text{ s}^{-1}$ and $k_{crys} = 0.600 \text{ s}^{-1}$. The diffusion coefficients in the paint and in the metal soap are $D_p = 5.100 \cdot 10^{-11} \text{ m}^2/\text{s}$ and $D_s = 3.635 \cdot 10^{-16} \text{ m}^2/\text{s}$, respectively, and the exponent defining the transition in the ionomer diffusion coefficient is $b = 2$. The calibrated parameters are summarised in Table 1. It is noted that the above calibration procedure somewhat differs from the calibration procedure applied in Hermans (2017). For most of the chemical model parameters this difference in the calibration procedure had a minor effect on the actual values obtained, as it should, with the exception being the value of D_s in Eq. (6). This difference, however, is consistent with a somewhat lower exponential value of $b = 2$ in Eq. (6). It may thus

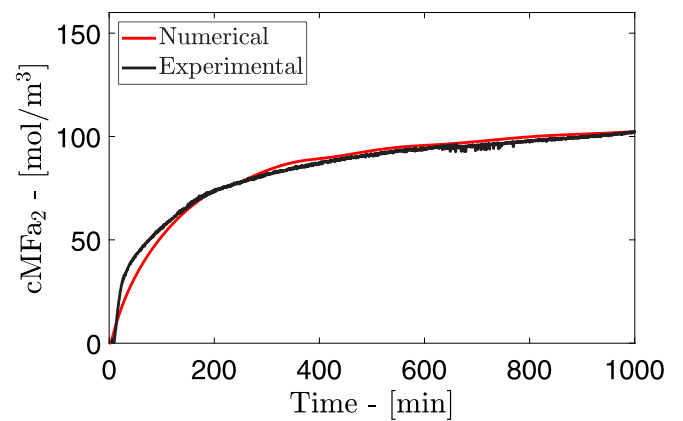


Fig. 6. Parameter calibration for the diffusion-reaction model. Time evolution (in minutes) of the concentration of crystalline lead soap (mol/m^3), as evaluated at the bottom of an ionomer sample, $x = l_{Fa} + l_s$. The black line represents the experimental result reported in Hermans (2017), and the red line reflects the numerical result for the one-dimensional model in Fig. 5(b) by solving Eq. (2) for the ionomer sample and Eq. (18) for the acetone-fatty acid solution. (For interpretation of the references to colour in this figure legend, the reader is referred to the web version of this article.)

be concluded that the calibrated parameters realistically represent the diffusion-reaction behaviour in the experimental system. Nevertheless, it should be mentioned that the presence of acetone in the experimental system promotes diffusion of saturated fatty acid in the ionomer film as well as swelling of the layer (Baij et al., 2018a), such that the calibrated diffusion parameters of the fatty acid in the ionomer overestimate those in a real historical painting. In order to quantitatively improve the model predictions, future research should aim at refining the estimated values of the input parameters by dedicated non-invasive experiments, or, when accurate experimental values are impossible to obtain, at investigating the sensitivity of the overall system behaviour to key parameter values or mechanistic assumptions.

4. Numerical example 1: Single-layer paint system

In this section a numerical example is analysed that is representative of degradation phenomena in oil paintings associated to the formation of multiple metal soap protrusions, as observed in historical paintings,

Table 1

Diffusion coefficients and reaction rates calibrated from the experiment reported in Hermans (2017) in which a palmitic acid diffuses and reacts in a lead-containing ionomer, in accordance with the representation in Fig. 5.

Parameter	Value	Unit
D_p	$5.100 \cdot 10^{-11}$	m^2/s
D_s	$3.635 \cdot 10^{-16}$	m^2/s
b	2	–
k_+	$0.491 \cdot 10^{-6}$	$\text{m}^6 (\text{mol}^2 \text{s})^{-1}$
k_-	0.169	s^{-1}
k_{cryst}	0.600	s^{-1}

see Fig. 1(a). The *single-layer paint system* studied consists of a lead white paint in which *three metal soap crystals* develop. The geometry is equal to that considered in Eumelen et al. (2021), which was analysed in accordance with the original chemical model introduced in Eumelen et al. (2019) that neglects the contribution of the amorphous metal soap in the chemical reaction process. Hence, a comparison between the results obtained with the original model and the current, enhanced model described in Section 2.1 allows to reveal the important contribution of the amorphous metal soap on the degradation process. Section 4.1 describes the geometry of the paint layer model, the material properties, and the initial and boundary conditions. The results of the numerical simulation are presented in Section 4.2.

4.1. Definition of the problem

4.1.1. Geometry and FEM discretisation

The single-layer paint system is modelled as a two-dimensional rectangular domain with a thickness $l = 15 \mu\text{m}$ and a width $4l = 60 \mu\text{m}$, in which three metal soap nuclei are present, see Fig. 7. The shape of the nuclei is taken as circular, with an initial radius equal to one tenth of the layer thickness, $r_0 = l/10 = 1.5 \mu\text{m}$. The finite element discretisation of the geometry is similar to that used in Eumelen et al. (2021), whereby, after a mesh convergence study, the element size close to the metal soap nuclei was set to $0.2 \mu\text{m}$, and at the corners of the geometry to $0.5 \mu\text{m}$, as required for obtaining mesh-independent numerical results. Accordingly, the computational domain is discretised with 27,030 continuum elements. For the diffusion–reaction analysis, 3-node isoparametric elements with a 3-point Gauss quadrature are used, while for the mechanical analysis 6-node plane-strain isoparametric elements with a 3-point Gauss quadrature are employed. The interface elements describing the discrete fracture processes in the FEM geometry are included by using a dedicated Python script, which first reduces the size of all the original continuum elements by 1%, then detects the opposing element edges, and subsequently places interface elements in between the continuum elements, leading to 40,345 interface elements in total. For the chemical analysis 4-node interface elements with a 2-point Gauss quadrature are used, and for the mechanical analysis 6-node interface elements with a 3-point Lobatto quadrature are selected. Note that the element formulation for the mechanical interface elements is not available in ABAQUS Standard, and is therefore incorporated by means of a user-defined element routine based to the numerical implementation presented in Schellekens and de Borst (1993). Finally, the radial detection distance used in the scanning algorithm for defining the thickness of the interfacial reaction zone from the integration points closest to the boundary of the crystalline metal soap is selected to be $0.2 \mu\text{m}$, which corresponds to the smallest characteristic element size in the FEM model. Hence, the radial detection distance is 7.5 times smaller than the initial radius r_0 of the metal soap nucleus, and 75 times smaller than the thickness l of the paint, and has a negligible influence on the computational results.

Table 2

Mechanical properties used in the *single-layer paint model* illustrated in Fig. 7.

Parameter	Value	Unit
Continuum elements		
Growth strain ϵ^{g}	0.077	–
Elastic modulus E_p, E_s	115	N/mm^2
Poisson's ratio ν_p, ν_s	0.3	–
Interface elements		
Fracture strength r_1^u, r_2^u	2.2	N/mm^2
Fracture toughness $G_{\text{I,c}}, G_{\text{II,c}}$	0.418	N/mm
Interface elastic stiffness K	10^6	N/mm^3

4.1.2. Material properties

The paint layer is assumed to be made of lead white paint. For the diffusion–reaction analysis the material properties obtained from the calibration procedure discussed in Section 3 have been used, as summarised in Table 1. The input parameters for the mechanical analysis are presented in Table 2. The Young's modulus of the lead white paint is extracted from the uniaxial stress–strain data presented in Fuster-López et al. (2016), leading to $E_p = 115 \text{ N}/\text{mm}^2$, and the Poisson's ratio is set to $\nu_p = 0.3$ (Eumelen et al., 2019). For the crystalline metal soap, no experimental data on the mechanical properties are available in the literature. Nevertheless, in Eumelen et al. (2019) it was demonstrated that the value of the mismatch between the stiffness of the metal soap crystal and that of the oil binder influences the growth characteristics of the metal soap crystal only marginally. Hence, for simplicity the elastic constants for the metal soap crystal are taken equal to those of the paint material, i.e., $E_p = E_s = 115 \text{ N}/\text{mm}^2$ and $\nu_p = \nu_s = 0.3$. The fracture properties of the paint and crystallised metal soap are derived from the stress–strain diagram reported in Fuster-López et al. (2016), leading to an ultimate tensile strength $r_1^u = 2.2 \text{ N}/\text{mm}^2$ and a mode I fracture toughness $G_{\text{I,c}} = 0.418 \text{ N}/\text{mm}$. From the simulation results presented in Eumelen et al. (2021), it can be observed that the fracture process in the painting is indeed dominated by mode I cracking events. Therefore, the fracture properties in mode II are expected to only have a minor influence on the computational results, and, for simplicity, are taken equal to the properties under mode I conditions, i.e., $r_2^u = r_1^u = 2.2 \text{ N}/\text{mm}^2$ and $G_{\text{II,c}} = G_{\text{I,c}} = 0.418 \text{ N}/\text{mm}$. The elastic stiffness of the interface elements is set to a relatively high value, $K = 10^6 \text{ N}/\text{mm}^3$, which, together with the choice of an appropriate mesh fineness, ensures that artificial response contributions related to the use of an elastic interface stiffness K in the traction–separation law are negligible, see Cid Alfaro et al. (2010a) for more details. Accordingly, the elastic response of the layer model is correctly determined by the continuum elements through the elastic properties of the paint and the crystalline metal soap.

To the best of the authors' knowledge, for the chemical growth strain associated to metal soap formation no experimental value has been reported in the literature. Hence, the value of $\epsilon^{\text{g}*} = 0.1$ pragmatically adopted for the plane-stress analyses presented in Eumelen et al. (2019, 2020, 2021) is adjusted for the current, plane-strain analysis by requiring that the effective, in-plane chemical growth strain in both 2D models is the same, which, in accordance with Equation (26) in Eumelen et al. (2019), is the case for $\epsilon^{\text{g}} = (1 + \nu_s)\epsilon^{\text{g}*} = (1 + 0.3) \cdot 0.1 = 0.077$. Note hereby that the choice of representing a 3D paint layer by a 2D plane-stress or plane-strain model is somewhat arbitrary, but, in principle, leads to comparable results for the in-plane chemo-mechanical behaviour of the paint layer.

4.1.3. Initial and boundary conditions

In the chemical model the initial concentration of saturated fatty acid is assumed to be uniform throughout the domain. The saturated fatty acid concentration has been calculated based on the composition of the lead white paint analysed in Fuster-López et al. (2016), which

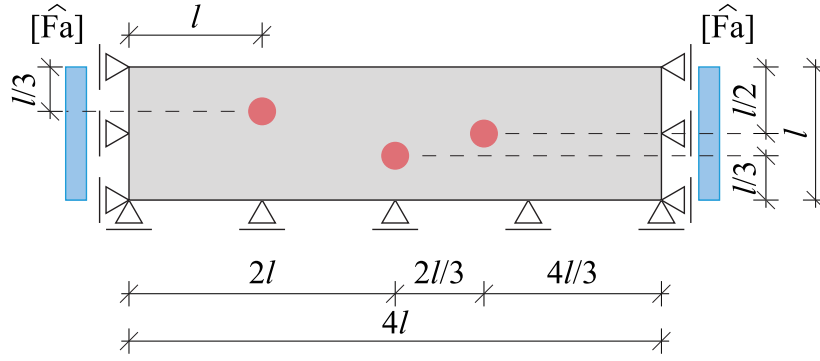


Fig. 7. Geometry and essential chemical and mechanical boundary conditions of the *single-layer paint system*, as taken from Eumelen et al. (2021). The grey area represents the paint layer and the three red circles indicate the metal soap nuclei present in the initial paint configuration. (For interpretation of the references to colour in this figure legend, the reader is referred to the web version of this article.)

contains stearic acids³ and lead-based pigments. The initial fatty acid concentration $[Fa](t = 0) = [Fa]_0$ is taken as *maximal* by assuming that *all* stearic acids from the binder are available for the formation of metal soap, in accordance with dividing the volumetric weight of the fatty acid in the oil binder by its molecular weight. The volumetric weight of the fatty acid is calculated by multiplying the volume fraction of linseed oil in a lead white paint ($=0.556$ (Fuster-López et al., 2016)) by its volumetric weight ($=930 \text{ kg/m}^3$ (Alfred, 2000)) and by the weight fraction of stearic acid in linseed oil ($=0.05$ (Alfred, 2000)). By adopting a molecular weight for the stearic acid of 0.2835 kg/mol (Anneken et al., 2012), an initial fatty acid concentration of $[Fa]_0 = 91 \text{ mol/m}^3$ is obtained.

The initial concentration of lead ions $[M](t = 0) = [M]_0$ is determined by assuming that only a specific *fraction* α of the lead ions present in the pigment particles reacts to form crystalline lead soap, see also the discussion below Fig. 3 in Section 1. For this purpose, consider the density of 6700 kg/m^3 of the lead white pigment (Lide, 2003) and the density of 1403 kg/m^3 of the lead stearate (i.e., lead soap) (Martínez-Casado et al., 2017). The molecular densities of lead white pigment and lead stearate follow from dividing these densities by the corresponding molecular weights, i.e., $\rho_{\text{pigment}} = 6700/0.776 = 8634 \text{ mol/m}^3$ for the lead white pigment and $\rho_s = 1403/0.774 = 1812 \text{ mol/m}^3$ for the lead stearate. From the chemical formula of lead white pigment, $2\text{PbCO}_3 \cdot \text{Pb}(\text{OH})_2$, it can be concluded that one mole of lead white pigment contains three moles of lead ions. Hence, the total molecular density of lead ions in lead white pigment is $\rho_{\text{Pb,pigment}} = 25902 \text{ mol/m}^3$. Consider now a unit volume of original lead white paint material $V_{\text{paint},0} = 1 \text{ m}^3$, which contains a volume fraction of 0.444 of lead white pigment (Fuster-López et al., 2016) and a volume fraction of $1 - 0.444 = 0.556$ of binder. The total number of moles of lead ions in the lead white pigment then becomes $N_{\text{Pb,pigment}} = 0.444 \times 25902 = 11500 \text{ mol}$. After the formation of lead soap, the *new* paint volume V_{paint} is obtained as the sum of the volume of remaining lead ions in the lead white pigment $V_{\text{Pb,pigment}}$, the volume of lead soap V_s , and the volume of the original binder material V_{bin} ($=0.556 \text{ m}^3$):

$$V_{\text{paint}} = V_{\text{Pb,pigment}} + V_s + V_{\text{bin}}. \quad (19)$$

The volume occupied by the lead soap follows from

$$V_s = \frac{\alpha N_{\text{Pb,pigment}}}{\rho_s}, \quad (20)$$

³ Note that the experiments presented in Hermans (2017), which in Section 3 are used to calibrate the parameters of the chemical model, are based on a palmitic acid solution. However, since the molecular weights of palmitic acid and stearic acid differ by only 10% (Anneken et al., 2012), it is expected that the chemical parameters calibrated in Section 3 realistically capture the diffusion–reaction behaviour of stearic acid.

where α is the fraction of lead ions available for the reaction into lead soap. The volume of the remaining lead ions in the paint then equals

$$V_{\text{Pb,pigment}} = \frac{(1 - \alpha) N_{\text{Pb,pigment}}}{\rho_{\text{Pb,pigment}}}. \quad (21)$$

The new paint volume can be calculated from the volumetric expansion induced by the free chemical growth strain $\varepsilon^{\text{g}*}$ as

$$\frac{V_{\text{paint}} - V_{\text{paint},0}}{V_{\text{paint},0}} = 1 + 3 \varepsilon^{\text{g}*}, \quad (22)$$

which, with $\varepsilon^{\text{g}*} = 0.1$ (Eumelen et al., 2019, 2020, 2021) and an original paint volume of $V_{\text{paint},0} = 1 \text{ m}^3$, leads to $V_{\text{paint}} = 1.3 \text{ m}^3$. Combining this result with Eqs. (19) to (21), and solving for α , results in $\alpha = 0.051$. Hence, the initial concentration of lead ions in 1 m^3 lead white paint that is available for the reaction into lead soap becomes $[M](t = 0) = [M]_0 = \alpha N_{\text{Pb,pigment}}/1 \text{ m}^3 = 587 \text{ mol/m}^3$.

In the simulations, it is realistic to assume that the initial concentration of lead ions is zero within the crystalline lead soap nuclei. In addition, the initial concentration of amorphous lead soap in the paint material is taken as zero, $[\text{aMFa}_2](t = 0) = [\text{aMFa}_2]_0 = 0 \text{ mol/m}^3$.

The chemical boundary conditions required for the diffusion–reaction analysis need to be prescribed in terms of the *diffusing* species, i.e., the saturated fatty acids. Accordingly, at the left and right domain boundaries the value of the initial concentration $[\hat{\text{F}}a] = [Fa]_0$ is imposed, see Fig. 7. Furthermore, at the top and bottom boundaries zero-flux boundary conditions are applied, $J_{\text{Fa}} = 0$. At the bottom of the paint layer this boundary condition reflects that the free saturated fatty acids do not penetrate the substrate below.

In the mechanical model the paint layer is initially considered to be stress-free. At the bottom boundary the vertical displacement is constrained, which represents the relatively stiff support provided to the paint by the wooden or canvas substrate. At the left and right boundary of the domain the horizontal displacement is prescribed to be zero. This boundary condition represents the upper limit for the horizontal deformation constraint provided by the paint material outside the computational domain. The top boundary of the domain is stress-free, in correspondence with zero-traction boundary conditions.

4.2. Results

For generality, the computational results are presented in terms of dimensionless parameters, with the dimensionless time defined as $\tilde{t} = t D_p / l^2$, where D_p and l are the diffusion coefficient in the paint material and the thickness of the paint layer, respectively. Since cracking in the paint occurs predominantly under mode I conditions, the local amount of cracking is assessed in terms of the normal (mode I) crack opening v_1 , which in dimensionless form reads $\tilde{v}_1 = v_1 / l$.

Fig. 8 depicts the deformed paint layer (with the deformation plotted at true scale) for different values of the dimensionless time \tilde{t} ,

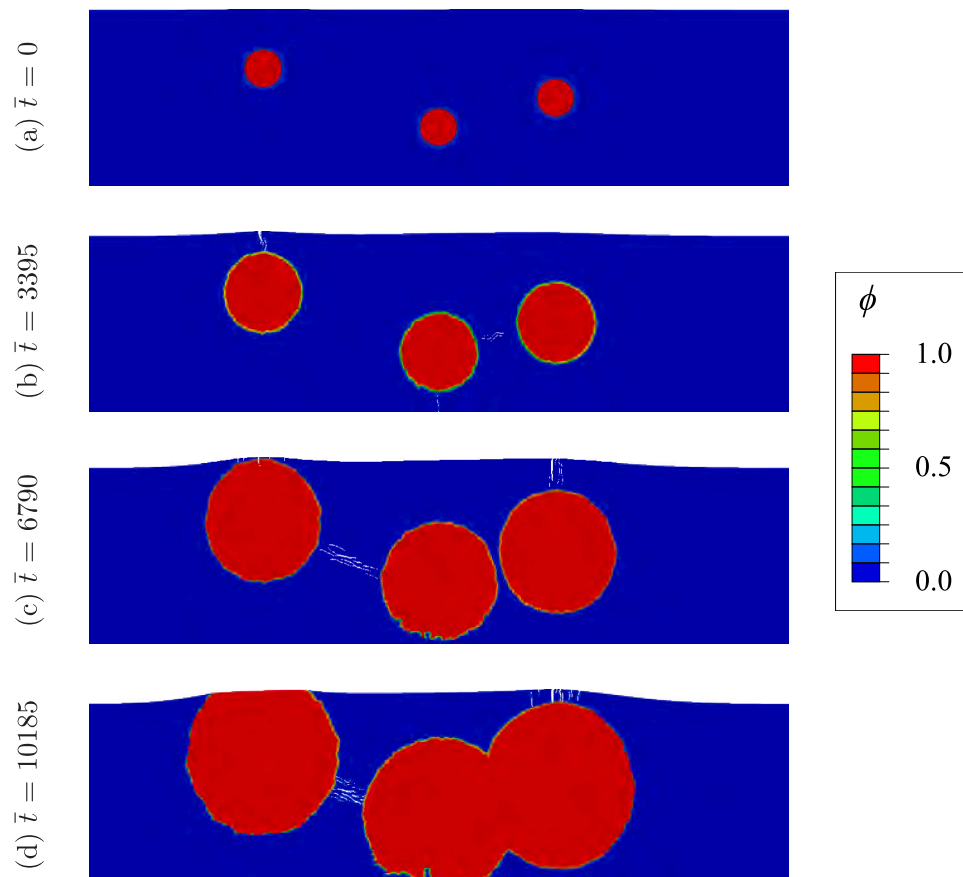


Fig. 8. *Single-layer paint system:* Time evolution (using the dimensionless time \bar{t}) of the paint configuration (with the deformation plotted at true scale), illustrating the growth of the metal soap crystals and the discrete crack patterns forming in the paint material. The contour plot variable ϕ refers to the volume fraction of crystalline metal soap, with the lower bound $\phi = 0$ designating the paint material (blue colour) and the upper bound $\phi = 1$ indicating the metal soap crystals (red colour). (For interpretation of the references to colour in this figure legend, the reader is referred to the web version of this article.)

thereby showing the progressive growth of the three metal soap nuclei and the formation of discrete cracks. The contour plot variable indicates the volume fraction ϕ of crystalline metal soap, with the red colour ($\phi = 1$) referring to fully crystallised metal soap and the blue colour ($\phi = 0$) designating the original paint material. The narrow reaction zones defining the transition from the paint material to a metal soap crystal are shown by the range of colours related to $0 < \phi < 1$. The growth of the metal soap crystals and the associated volumetric expansion clearly cause an upward deflection of the upper surface of the paint layer. This is particularly evident at the left crystal, which is able to reach the upper part of the paint layer and then erupts through the outer surface. It can be further seen that the three crystals initially grow at approximately the same rate and develop a circular shape, see Figs. 8(a), (b) and (c). Note that this shape closely resembles that of the metal soaps visible in the cross-sectional image taken from the ceiling painting in the Room of Trustees, Burgerweeshuis, Zierikzee, see Fig. 1(a). Nevertheless, at the largest time instant considered, $\bar{t} = 10185$, the central and right crystals have coalesced into a single, elongated metal soap aggregate, see Fig. 8(d). This elongated shape shows resemblance with that of the metal soap crystals observed in *View of Delft* by Johannes Vermeer, see Fig. 1(b), although the approximate crystal size of $100 \mu\text{m}$ observed in this painting is somewhat larger than the maximal crystal size of $25 \mu\text{m}$ following from the numerical simulation. Trivially, the maximum crystal size is determined by the specific time frame and the paint layer geometry considered in the analysis.

During the process of metal soap growth, discrete cracks are initiated once the stress in the paint material attains the fracture strength. As illustrated in Fig. 8(c), near the top surface of the paint layer, just above the left metal soap crystal, 6 distinct mode I cracks develop.

The time evolution of the dimensionless normal crack opening $\bar{v}_1 = v_1/l$ of the 4 largest mode I cracks is shown in Fig. 9(a), and is evaluated at the upper surface of the paint layer at which the crack mouth opening is maximal. As shown in Figs. 8(b) and (c), the first surface crack nucleates close to the vertical symmetry line of the left metal soap crystal, and partly penetrates the crystal. The additional surface cracks develop in the paint material region adjacent to the first surface crack, see Fig. 8(c), thereby inducing a further relaxation of the tensile stresses at the paint surface. When the left metal soap crystal approaches the tips of these surface cracks, the cracks start to close, due to compressive stresses generated in the crystal by restrained volumetric expansion originating from the chemical growth strain, see Eq. (9). As illustrated in Fig. 9(a), the completion of crack closure occurs at approximately the same time instant for all 4 surface cracks. Note further from Figs. 8(c) and (d) that similar mode I surface cracks develop above the right metal soap crystal, although later in time. In addition, diffusive patterns of micro-cracks are generated in between the three metal soap crystals, which occurs along trajectories directing towards their geometrical centres, see Figs. 8(b), (c) and (d). As for the surface cracks, crack closure is observed once the metal soap crystals approach these micro-cracks, see Fig. 8(d).

In order to reveal the specific influence of the enhanced chemical model on the growth processes of the crystalline metal soaps and the discrete cracks, the present numerical results are compared to those in Eumelen et al. (2021) that are based on the original model proposed in Eumelen et al. (2019), which, as mentioned, neglects the reversible reaction of amorphous metals soaps and only accounts for the formation of irreversible, crystalline metal soap. The numerical simulation presented in Eumelen et al. (2021) starts from the same

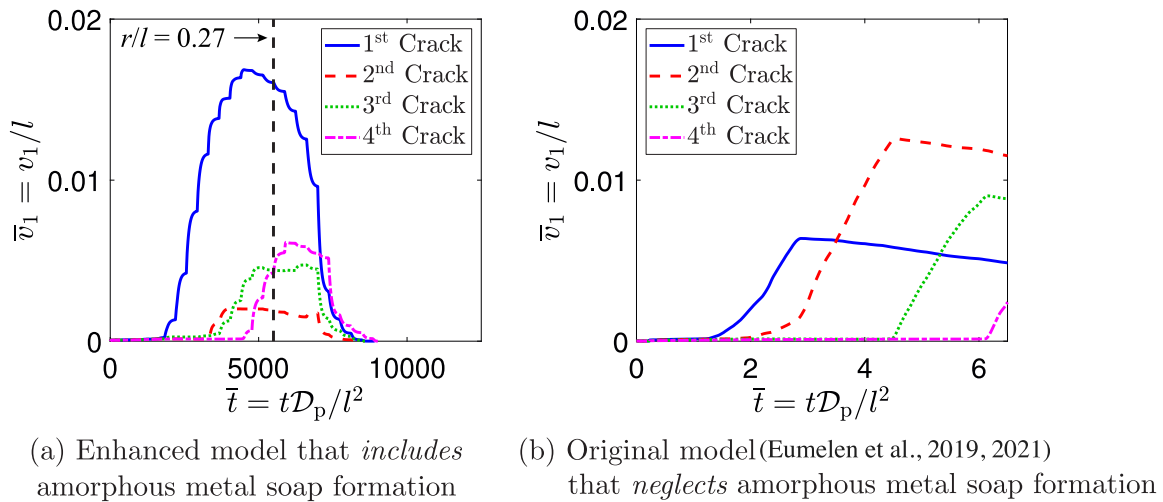


Fig. 9. *Single-layer paint system:* Time evolution (using the dimensionless time \bar{t}) of the normalised crack opening \bar{v}_1 of 4 dominant mode I surface cracks that develop above the left metal soap crystal, as predicted by (a) the current, enhanced model that *includes* the formation of amorphous metal soap, and (b) the original model presented in Eumelen et al. (2019, 2021) that *neglects* the formation of amorphous metal soap. The vertical dashed line in Fig. 9(a) designates the specific time $\bar{t} = 5500$ at which the left metal soap crystal shown in Fig. 8 reaches a relative size of $\bar{r} = r/l = 0.27$, which corresponds to the final crystal size reached at $\bar{t} = 6.5$ in the simulation considered in Fig. 9(b).

initial configuration as that displayed in Fig. 8(a), and shows that the growth rate and final size and shape of the three metal soap crystals strongly depend on their precise location in the computational domain. Specifically, the two outer metal soap crystals eventually obtain a slightly oval-shaped geometry that is almost two times larger in size than that of the central, circular metal soap crystal, see Figure 4 in Eumelen et al. (2021). This result is rather different from that shown in Fig. 8, and can be ascribed to the fact that, by ignoring the intermediate amorphous metal soap phase, in the original model the free saturated fatty acid is consumed at a *significantly higher rate*, whereby its spatial distribution, and thus the corresponding development of metal soaps crystals, becomes non-uniform across the paint layer, see Figure 6 in Eumelen et al. (2021). Conversely, the relatively low rate at which the free fatty acid is consumed in the current, enhanced model ensures that its spatial distribution remains uniform when time develops, thus resulting in a virtually homogeneous growth of the three individual metal soap crystals (as long as they do not coalesce).

The fracture response in Fig. 9(a) is now compared to that in Fig. 9(b), which illustrates the time evolution of the dimensionless normal crack opening $\bar{v}_1 = v_1/l$ of the 4 main surface cracks as computed by the original model that neglects amorphous metal soap formation. The 4 surface cracks considered in Fig. 9(b) are located above the left metal soap crystal, at comparable locations as shown in Fig. 8 for the enhanced model, and appear to have similar crack widths as those in Fig. 9(a). The simulation carried out with the original model covers a total time of $\bar{t} = 6.5$, at which the normalised average radius of the left metal soap crystal has reached a value of $\bar{r} = r/l = 0.27$. For a proper comparison with the enhanced model, in Fig. 9(a) the simulation time corresponding to this crystal size has been indicated by a vertical dashed line. It can be observed that the vertical dashed line is related to a dimensionless time of $\bar{t} = 5500$, which is about a factor of 850 larger than the dimensionless time $\bar{t} = 6.5$ at which the crystal size $\bar{r} = r/l = 0.27$ is reached in the original model. In addition, Fig. 9(a) illustrates that for the enhanced model the time at which the first surface crack nucleates is approximately 1300 times larger than for the original model in Fig. 9(b). This again confirms that the addition of the amorphous metal soap phase in the enhanced model substantially delays the formation of crystalline metal soap, and thus the generation of discrete cracks, and shows that the characteristic time scale associated to the chemo-mechanical degradation of the single paint layer is increased by approximately three orders of magnitude. Specifically, from the definition of the dimensionless time $\bar{t} = tD_p/l^2$, it follows that in the enhanced model the metal soap formation process

occurs over a time frame of hours to days, while in the original model it takes place over a time frame of seconds to minutes.

Although the characteristic time scale computed by the current, enhanced model is in agreement with that of the experiments reported in Hermans (2017), see also Fig. 6, it is still significantly smaller than the time scale of years to decades characterising metal soap degradation processes of historical paintings in museum collections. This difference can be ascribed to the relatively high concentration value used in the definition of the initial and boundary conditions for the saturated fatty acid. As described in Section 4.1.3, the initial and boundary conditions imposed are representative of the *maximum* saturated fatty acid concentration available for the chemical reaction process; in specific, it is assumed that *all* stearic acids from the binder are available for the formation of metal soap. It is further assumed that this maximum concentration is already present in the paint layer from the beginning of the simulation. In real, historical paintings, however, the concentrations of saturated fatty acids and metal ions gradually build up in paint layers as a result of the drying process of the paint, which typically takes place over a period of years to decades (Baij et al., 2019; Hermans et al., 2015, 2016a; Baij et al., 2018a; Mecklenburg et al., 2004). The analysis of the dependency of the characteristic time scale of the chemo-mechanical degradation process on the drying process of paint is considered to be a topic for future research.

5. Numerical example 2: Multi-layer paint system

In this section the influence of the formation of a *single lead soap crystal* on cracking and delamination in a *multi-layer paint system* is analysed. The geometry, material properties, and initial and boundary conditions of the multi-layer model are presented in Section 5.1, and the results of the numerical simulations are discussed in Section 5.2.

5.1. Definition of the problem

5.1.1. Geometry and FEM discretisation

The geometry of the multi-layer paint system is characterised by a $2l \times 2l$ square domain whereby $l = 50 \mu\text{m}$, which is composed of a ground layer indicated as *layer 1*, and a pictorial layer indicated as *layer 2*, see Fig. 10. The ground layer is made of lead white paint and has a thickness $l_1 = 85 \mu\text{m}$, while the pictorial layer consists of cobalt blue paint and has a thickness $l_2 = 15 \mu\text{m}$. Note that the cobalt blue paint has been chosen as a representative paint material that does not contain

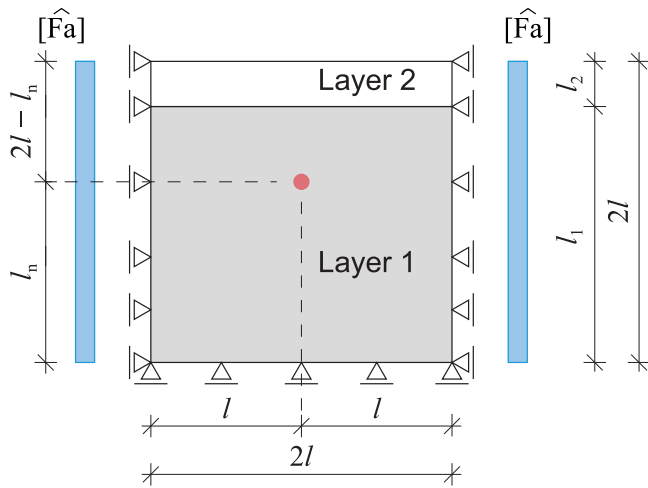


Fig. 10. Geometry and essential chemical and mechanical boundary conditions for the *multi-layer paint system*. In the ground layer (layer 1, grey colour) lead ions are present, while in the pictorial layer (layer 2, white colour) no lead ions are present. The red circle indicates the lead soap nucleus initially present in the ground layer. (For interpretation of the references to colour in this figure legend, the reader is referred to the web version of this article.)

lead ions. The ground layer contains a single, circular lead soap nucleus with an initial radius $r_0 = 1.5 \mu\text{m}$, which is located along the vertical symmetry axis of the domain, at a distance $l_n = 60 \mu\text{m}$ from the bottom of the paint system. The modelled domain is discretised by using 44,856 continuum elements and 67,185 interface elements. The element types applied in the simulation are the same as those selected for the single-layer model, see Section 4.1.1 for more details. The minimum element size is applied close to the lead soap nucleus and equals $0.2 \mu\text{m}$. The maximum element size taken at the left and right domain boundaries is $5 \mu\text{m}$. The radial detection distance used in the scanning algorithm for defining the thickness of the interfacial reaction zone between the lead soap crystal and the paint material is $0.4 \mu\text{m}$. It has been confirmed that for the chosen mesh density the numerical results converge within a small, specified tolerance.

5.1.2. Material properties

The material properties in the chemical model are presented in Table 1, as obtained from the calibration procedure presented in Section 3. For simplicity, the diffusion coefficients of the free saturated fatty acids in the ground layer and in the pictorial layer are taken the same.

The material parameters used in the mechanical model are listed in Table 3. For the ground layer (layer 1), the elastic modulus is derived from the uniaxial stress–strain response of an 18.75 year old lead white paint (Mecklenburg et al., 2012), leading to $E_p = 130 \text{ N/mm}^2$. For the pictorial layer (layer 2), the elastic modulus is obtained from the stress–strain response of an 18 year old cobalt blue paint presented in Fuster-López et al. (2019), resulting in $E_p = 35 \text{ N/mm}^2$. The Poisson's ratio is taken the same for the two paint layers and equals $\nu_p = 0.3$. Since it is assumed that there are no lead ions present in layer 2, lead soap growth can only occur in layer 1, whereby the elastic properties of the lead soap crystal are taken the same as those of the lead white paint, $E_s = E_p = 130 \text{ N/mm}^2$ and $\nu_s = \nu_p = 0.3$. The ultimate tensile strength of the lead white paint is obtained from the uniaxial stress–strain data presented in Mecklenburg et al. (2012), resulting in $t_1^u = 4.5 \text{ N/mm}^2$. The mode I toughness of the lead white paint is derived from the area under the uniaxial stress–displacement response – with the displacement determined as the strain multiplied by the gauge length $l_g = 76 \text{ mm}$ (M. Mecklenburg, personal communication) –, leading to $G_{I,c} = 7.86 \text{ N/mm}$. Similarly, the ultimate tensile strength and mode I

Table 3

Mechanical properties used in the *multi-layer paint model* illustrated in Fig. 10.

Parameter	Value	Unit
<i>Lead white ground layer (layer 1)</i>		
Continuum elements		
Growth strain ε^g	0.077	–
Elastic modulus E_p, E_s	130	N/mm ²
Poisson's ratio ν_p, ν_s	0.3	–
Interface elements		
Fracture strength t_1^u, t_2^u	4.5	N/mm ²
Fracture toughness $G_{I,c}, G_{II,c}$	7.86	N/mm
Interface elastic stiffness K	10^6	N/mm ³
<i>Cobalt blue pictorial layer (layer 2)</i>		
Continuum elements		
Elastic modulus E_p	35	N/mm ²
Poisson's ratio ν_p	0.3	–
Interface elements		
Fracture strength t_1^u, t_2^u	0.35	N/mm ²
Fracture toughness $G_{I,c}, G_{II,c}$	0.033	N/mm
Interface elastic stiffness K	10^6	N/mm ³

toughness of the cobalt blue paint follow from the experimental data presented in Fuster-López et al. (2019), leading to $t_1^u = 0.35 \text{ N/mm}^2$ and $G_{I,c} = 0.033 \text{ N/mm}$, with the latter value calculated using the applied gauge length of $l_g = 7.5 \text{ mm}$. For simplicity, for both layers the mode I and mode II fracture properties are taken the same, $t_2^u = t_1^u$ and $G_{II,c} = G_{I,c}$. As for the single-layer paint model analysed in Section 4, the growth strain is selected as $\varepsilon^g = 0.077$ and the elastic stiffness in the interface damage model equals $K = 10^6 \text{ N/mm}^3$. Finally, the fracture properties of the delaminating cracks that may develop along the material interface between the ground layer and the pictorial layer are assumed to be equal to the fracture properties of the pictorial layer (layer 2), which is the weaker, more brittle layer.

5.1.3. Initial and boundary conditions

The initial conditions and boundary conditions adopted for the multi-layer paint model are comparable to those applied for the single-layer paint model discussed in Section 4.1.3. In the chemical model the initial concentration of free saturated fatty acid is assumed to be uniform throughout the domain and equals $[\text{Fa}]_0 = 91 \text{ mol/m}^3$. The initial concentration of lead ions is taken as uniform in the lead white ground layer (layer 1), and equals $[\text{M}]_{0,1} = 587 \text{ mol/m}^3$. As mentioned, no lead ions are present in the cobalt blue pictorial layer (layer 2), in correspondence with $[\text{M}]_{0,2} = 0$. The initial concentrations of the amorphous and crystalline metal soaps are assumed to be equal to zero, i.e., $[\text{aMFA}_2]_0 = [\text{cMFA}_2]_0 = 0 \text{ mol/m}^3$. The above value for the initial concentration of free saturated fatty acid $[\text{Fa}]_0$ is also imposed at the left and right boundaries of the computational domain. Furthermore, at the top and bottom boundaries of the domain zero-flux boundary conditions are adopted for the saturated fatty acid, $J_{\text{Fa}} = 0$.

Similar to the single-layer paint model studied in Section 4, in the mechanical model the multi-layer paint system is initially considered to be stress-free. The vertical displacement is prevented at the bottom boundary of the domain, while at the left and right boundaries the horizontal displacement is constrained. Finally, the top boundary is stress-free, in correspondence with zero-traction boundary conditions.

5.2. Results

Fig. 11 shows the progressive growth of the lead soap crystal and the cracks and interfacial delamination generated in the multi-layer paint system, considering 4 different values of the dimensionless time \bar{t} (with the deformation plotted at true scale). The dimensionless time is defined as $\bar{t} = tD_p/l^2$, with $l = 50 \mu\text{m}$ taken as half of the total model thickness of the paint system, see also Fig. 10. The contour plot variable indicates the volume fraction of crystalline lead soap ϕ , with the red

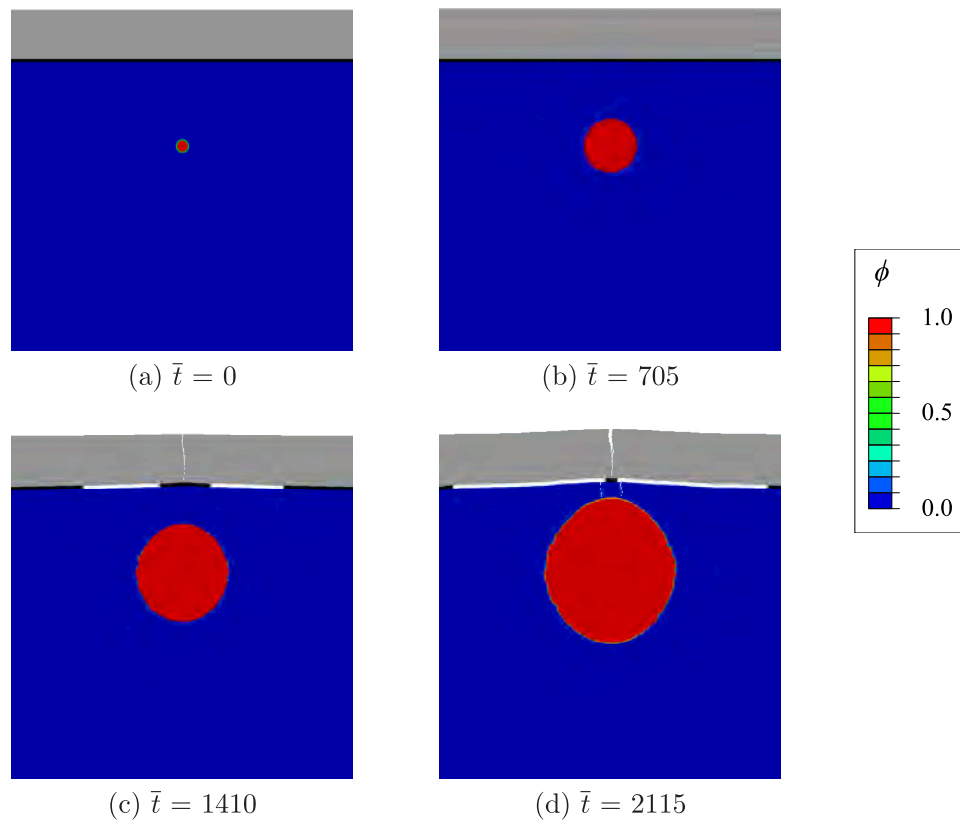


Fig. 11. *Multi-layer paint system:* Time evolution (using the dimensionless time \bar{t}) of the paint configuration (with the deformation plotted at true scale), illustrating the growth of the lead soap crystal and the discrete cracks and delamination processes forming in the paint system. The contour plot variable ϕ refers to the volume fraction of crystalline lead soap. The black lines indicate the intact interface between the ground and the paint layers and the white lines designate two symmetrical, delaminating cracks at the interface. The grey area above the interface indicates layer 2, in which no lead ions are present and therefore does not contribute to the formation of metal soap. (For interpretation of the references to colour in this figure legend, the reader is referred to the web version of this article.)

colour referring to the fully crystallised lead soap ($\phi = 1$) and the blue colour reflecting the original paint material ($\phi = 0$). The top grey layer indicates layer 2, in which no lead ions are present, and therefore does not contribute to the formation of lead soap. In addition, the intact interface between the ground layer (layer 1) and the pictorial layer (layer 2) is designated by the black horizontal lines, and the white lines in Figs. 11(c) and (d) indicate two symmetrical, delaminating cracks emerging at the layer interface.

The lead soap crystal develops with a circular shape in the ground layer, see Figs. 11(a) and (b), and generates a mode I surface crack in the upper, pictorial layer when approaching the interface between the two layers, see Figs. 11(c) and (d). The volumetric expansion caused by the chemical growth strain induces an upward deflection of the upper, free surface of the paint system. In combination with the mismatch in the material properties of the ground layer and pictorial layer, relatively large shear stresses develop along the layer interface, which result in the nucleation and growth of two symmetrical, mode II delaminating cracks (indicated by the white lines). It can be seen from Fig. 11(d) that the delaminating cracks are close to coalescence once the mode I surface crack has grown through the entire thickness of the upper, pictorial layer, thereby forming a T-shape crack with the mode I surface crack. T-shape cracks are regularly observed in historical paintings, and may originate from metal soap formation and/or indoor climate fluctuations, often leading to local paint flaking and paint loss (Bosco et al., 2020, 2021).

Fig. 12(a) presents the time evolution of the normalised normal crack opening $\bar{v}_1 = v_1/l$ of the mode I crack surface crack, as evaluated at the surface of the upper, pictorial layer at which the crack mouth opening is maximal. It can be seen that the crack grows at an approximately constant rate. Contrary to what occurs in the single-layer

paint system, see Fig. 9(a), crack closure does not occur within the time frame considered. This is due to the fact that the compressive stress caused by the constrained volumetric expansion of the lead soap crystal has partially relaxed as a result of the formation of the two mode II delaminating cracks at the layer interface, and that the lead soap crystal is not able to penetrate the upper pictorial layer due to the absence of lead ions in this layer.

Fig. 12(b) illustrates the time evolution of the two mode II delaminating cracks that develop along the layer interface, expressed in terms of the normalised delamination length, $\bar{l}_d = l_d/l$ with l_d the actual delamination length. Observe that the delaminating cracks grow in a synchronous (symmetrical) fashion at an initially high rate, but that the growth rate decreases substantially when time develops. As illustrated in Figs. 12(c) and (d), the decrease in growth rate may be caused by the fact that the delaminations get closer to the mode I surface crack with increasing time, thereby reaching a region in which the stress cannot grow, such that the driving force for further delamination decreases.

It is finally noted that the small, staircase increments characterising the fracture responses in Fig. 12 result from the discrete interplay between the local element size and the radial detection distance used in the scanning algorithm for defining the thickness of the interfacial reaction zone. Indeed, in the limit of an infinitesimal element size and an infinitesimal reaction zone, the fracture responses in Fig. 12 are expected to become ideally smooth.

6. Conclusions

This paper proposes a chemo-mechanical model for the prediction of degradation phenomena in historical oil paintings as induced by metal soap reactions, such as the formation of metal soap aggregates,

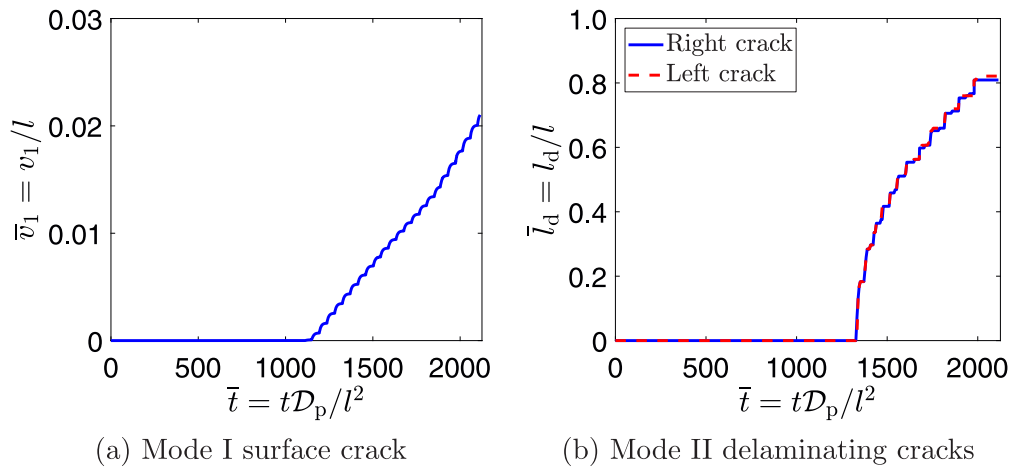


Fig. 12. *Multi-layer paint system*: Time evolution (using the dimensionless time \bar{t}) of (a) the normalised crack opening \bar{v}_1 of the mode I surface crack, and (b) the normalised delamination length \bar{l}_d of the two mode II delaminating cracks developing along the layer interface.

the deformation of the paint surface, paint cracking, and delamination between paint layers. Departing from the framework presented in an earlier work (Eumelen et al., 2019), the chemical model has been substantially enhanced to describe *both* the reversible reaction between free saturated fatty acids and metal ions forming amorphous metal soap, and the irreversible reaction into crystalline metal soap. The chemical parameters of the *enhanced chemo-mechanical model* have been calibrated on the experimental results published in Hermans (2017) that measure the time evolution of the concentration of crystalline metal soap forming from a lead-containing ionomer exposed to a fatty acid solution. Metal soap crystallisation introduces stresses in the paint that promote crack nucleation and propagation; this discrete cracking behaviour of the paint is simulated by surrounding the continuum elements in the finite element model with interface elements equipped with a mixed-mode interface damage model, which allows for the robust simulation of crack patterns at arbitrary locations and in arbitrary directions.

The enhanced chemo-mechanical damage model has been applied for analysing two types of boundary value problems, which capture the essential degradation mechanisms observed in historical oil paintings in museum collections. The first boundary value problem concerns the deformation and fracture response of a *single-layer paint system* under the growth of *multiple metal soap crystals*. The computational results show that the growth of the metal soap crystals and the associated volumetric expansion cause a substantial upward deflection of the top surface of the paint layer and induce multiple cracks at the layer surface and in between the individual metal soap crystals. The growth rate of the three metal soap crystals is independent of their location within the domain, which is due to the homogeneous spatial development of the fatty acid concentration in time. Further, at some stage two different metal soap crystals coalesce into a single, oval-shape metal soap aggregate that is characteristic for metal soaps observed in real, historical paintings.

The modelling results are compared to those presented in Eumelen et al. (2021) that were computed by the original chemo-mechanical model presented in Eumelen et al. (2019), which neglects the intermediate, amorphous metal soap phase and only accounts for the irreversible chemical reaction into crystalline metal soap. From this comparison, it follows that the inclusion of the intermediate, amorphous metal soap phase in the model formulation increases the characteristic time scale associated to the chemo-mechanical degradation process by three orders of magnitude, which is necessary to realistically predict the time-dependency of degradation processes observed in historical paintings in museum collections. Also, local differences are observed in the metal soap growth characteristics and crack profiles

predicted by the two models, which are caused by the fact that with the current, enhanced chemo-mechanical model the saturated fatty acid profile develops homogeneously across the paint layer, while with the original chemo-mechanical model this occurs in a heterogeneous fashion.

The second boundary value problem considers the deformation, cracking and delamination processes in a *multi-layer paint system*, as induced by the growth of a *single lead soap crystal*. The multi-layer paint system is composed of a pictorial layer that is supported by a ground layer containing a lead soap nucleus. The growth of the lead soap nucleus induces a significant upward deformation of the paint surface. In addition, a mode I surface crack develops across the thickness of the upper, pictorial layer, which coalesces with two symmetrical delaminations developing along the layer interface, thereby forming a T-shape crack that ultimately may lead to local paint flaking and paint loss.

The enhanced chemo-mechanical formulation and modelling results presented in this communication provide a better understanding of the coupled chemo-mechanical degradation behaviour of historical oil paintings due to metal soap formation. Future research will aim at refining the model input parameters by, for example, accurately determining the mechanical parameters of small paint samples taken from historical paintings via nanoindentation testing (Salvant et al., 2011; Freeman et al., 2019; Fujisawa and Łukowski, 2019; Tiennot et al., 2020; Eumelen et al., 2022). Additionally, the effects of conservation treatments (Baij et al., 2019), indoor climate conditions (Keune et al., 2016), and paint drying characteristics (Mecklenburg et al., 2004) on the process of metal soap degradation need to be explored in more detail. The interaction between metal soap-induced degradation mechanisms and climate-induced failure of historical paintings (Bosco et al., 2020, 2021) is another topic for future study. Such investigations eventually should lead to optimal preventive conservation measures and environmental display/storage conditions required for preserving valuable historical paintings for future generations.

CRediT authorship contribution statement

G.J.A.M. Eumelen: Software, Formal analysis, Methodology, Resources, Writing – original draft. **E. Bosco:** Conceptualization, Methodology, Writing – original draft, Supervision, Funding acquisition, Project administration. **A.S.J. Suiker:** Conceptualization, Methodology, Writing – original draft, Supervision. **J.J. Hermans:** Conceptualization, Resources, Writing – review & editing.

Declaration of competing interest

The authors declare that they have no known competing financial interests or personal relationships that could have appeared to influence the work reported in this paper.

Data availability

Data will be made available on request.

Acknowledgements

E.B. is grateful for the support by the Netherlands Organisation for Scientific Research (NWO), Project 15873, “Engineering goes Beauty - A computational multi-physics modelling approach towards the preservation of historical oil paintings”, within the funding scheme “NWO Veni Award”. A.S.J.S. gratefully acknowledges the support of the European Union’s Horizon 2020 research and innovation programme CollectionCare (Perles et al., 2020), under grant agreement N. 814624. J.J.H. is grateful for the support by the Netherlands Organisation for Scientific Research (NWO), Project 016.Veni.192.052.

References

- Alfred, T., 2000. Fats and Fatty Oils. Ullmann’s Encyclopedia of Industrial Chemistry, pp. 1–72.
- Anneken, D., Both, S., Christoph, R., Fieg, G., Steinberner, U., Westfachtel, A., 2012. Fatty Acid. Ullmann’s Encyclopedia of Industrial Chemistry, pp. 73–116.
- Baij, L., Chassouant, L., Hermans, J.J., Keune, K., Iedema, P.D., 2019. The concentration and origins of carboxylic acid groups in oil paint. *RSC Adv.* 9 (61), 35559–35564.
- Baij, L., Hermans, J.J., Keune, K., Iedema, P.D., 2018a. Time-dependent ATR-FTIR spectroscopic studies on fatty acid diffusion and the formation of metal soaps in oil paint model systems. *Angew. Chem., Int. Ed. Engl.* 57 (25), 7351–7354.
- Baij, L., Hermans, J.J., Keune, K., Iedema, P.D., 2018b. Time-dependent ATR-FTIR spectroscopic studies on solvent diffusion and film swelling in oil paint model systems. *Macromolecules* 51 (18), 7134–7144.
- Beerse, M., Keune, K., Iedema, P.D., Woutersen, S., Hermans, J.J., 2020. Evolution of zinc carboxylate species in oil paint ionomers. *Appl. Polym. Mater.* 2 (12), 5674–5685.
- Bonaduce, I., Carlyle, L., Colombini, M.P., Duce, C., Ferrari, C., Ribecchini, E., Selleri, P., Tiné, M.R., 2012. New insights into the ageing of linseed oil paint binder: A qualitative and quantitative analytical study. *PLOS ONE* 7 (11), 1–14.
- Bonaduce, I., Duce, C., Lluveras-Tenorio, A., Lee, J., Ormsby, B., Burnstock, A., van den Berg, K.J., 2019. Conservation issues of modern oil paintings: a molecular model on paint curing. *Acc. Chem. Res.* 52, 3397–3406.
- Boon, J.J., van der Weerd, J., Keune, K., Noble, P., Wadum, J., 2003. Mechanical and chemical changes in old master paintings: dissolution, metal soap formation and remineralization processes in lead pigmented ground/intermediate paint layers of 17th century painting. In: Vontobel, R. (Ed.), 13th Triennial Meeting of the ICOM Committee for Conservation in Rio de Janeiro. James & James, London, pp. 401–406.
- Bosco, E., Suiker, A.S.J., Fleck, N.A., 2020. Crack channelling mechanisms in brittle coating systems under moisture or temperature gradients. *Int. J. Fract.* 225, 1–30.
- Bosco, E., Suiker, A.S.J., Fleck, N.A., 2021. Moisture-induced cracking in a flexural bilayer with application to historical paintings. *Theor. Appl. Fract. Mech.* 112, 102779.
- Chen-Wiegart, Y.K., Catalano, J., Williams, G.J., Murphy, A., Yao, Y., Zumbulyadis, N., Centeno, S.A., Dybowski, C., Thieme, J., 2017. Elemental and molecular segregation in oil paintings due to lead soap degradation. *Sci. Rep.* 7, 11656.
- Cid Alfaro, M.V., Suiker, A.S.J., de Borst, R., 2010a. Transverse failure behavior of fiber-epoxy systems. *J. Compos. Mater.* 44 (12), 1493–1516.
- Cid Alfaro, M.V., Suiker, A.S.J., de Borst, R., Remmers, J.J.C., 2009. Analysis of fracture and delamination in laminates using 3D numerical modelling. *Eng. Fract. Mech.* 76 (6), 761–780.
- Cid Alfaro, M.V., Suiker, A.S.J., Verhoosel, C.V., de Borst, R., 2010b. Numerical homogenization of cracking processes in thin fibre-epoxy layers. *Eur. J. Mech. A Solids* 29 (2), 119–131.
- Cotte, M., Checroun, E., Nolf, W.D., Taniguchi, Y., Viguerie, L.D., Burghammer, M., Walter, P., Rivard, C., Salomé, M., Janssens, K., Susini, J., 2017. Lead soaps in paintings: Friends or foes? *Stud. Conserv.* 62 (1), 2–23.
- Cotte, M., Checroun, E., Susini, J., Dumas, P., Tchoreloff, P., Besnard, M., Walter, P., 2006. Kinetics of oil saponification by lead salts in ancient preparations of pharmaceutical lead plasters and painting lead mediums. *Talanta* 70, 1136–1142.
- Cotte, M., Checroun, E., Susini, J., Walter, P., 2007. Micro-analytical study of interactions between oil and lead compounds in paintings. *Appl. Phys. A* 89, 841–848.
- Erhard, D., Tumosa, C.S., Mecklenburg, M.F., 2005. Long-term chemical and physical processes in oil paint films. *Stud. Conserv.* 50 (2), 143–150.
- Eumelen, G.J.A.M., Bosco, E., Suiker, A.S.J., Hermans, J.J., van Loon, A., Iedema, P.D., Keune, K., 2021. Numerical modeling of metal soap formation and microcracking in historical oil paintings. In: Bridgland, J. (Ed.), *Transcending Boundaries: Integrated Approaches to Conservation*. International Council of Museums, ICOM-CC 19th Triennial Conference Preprints, Beijing, 17–21 May 2021.
- Eumelen, G.J.A.M., Bosco, E., Suiker, A.S.J., Hermans, J.J., van Loon, A., Keune, K., Iedema, P.D., 2020. Computational modelling of metal soap formation in historical oil paintings: the influence of fatty acid concentration and nucleus geometry on the induced chemo-mechanical damage. *SN Appl. Sci.* 2, 1310.
- Eumelen, G.J.A.M., Bosco, E., Suiker, A.S.J., van Loon, A., Iedema, P.D., 2019. A computational model for chemo-mechanical degradation of historical oil paintings due to metal soap formation. *J. Mech. Phys. Solids* 132, 103683.
- Eumelen, G.J.A.M., Suiker, A.S.J., Bosco, E., Fleck, N.A., 2022. Analytical model for elasto-plastic indentation of a hemispherical surface inclusion. *Int. J. Mech. Sci.* 224, 107267.
- Freeman, A., Lukomski, M., Beltran, V., 2019. Mechanical characterization of a cross-sectional TiO₂ acrylic-based paint by Nano-indentation. *J. Am. Inst. Conserv.* 1–13.
- Fujisawa, N., Lukomski, M., 2019. Nanoindentation near the edge of a viscoelastic solid with a rough surface. *Mater. Des.* 184, 108174.
- Fuster-López, L., Izzo, F.C., Damato, V., Yusà-Marco, D.J., Zendri, E., 2019. An insight into the mechanical properties of selected commercial oil and alkyd paint films containing cobalt blue. *J. Cultural Herit.* 35, 225–234.
- Fuster-López, L., Izzo, F.C., Piovesan, M., Yusà-Marco, D.J., Sperti, L., Zendri, E., 2016. Study of the chemical composition and the mechanical behaviour of 20th century commercial artists’ oil paints containing manganese-based pigments. *Microchem. J.* 124, 962–973.
- Geng, F., Suiker, A.S.J., 2019. An interface damage model for high-cycle fatigue. *Eng. Fract. Mech.* 221, 106644.
- Hagan, E.W., 2017. Thermo-mechanical properties of white oil and acrylic artist paints. *Prog. Org. Coat.* 104, 28–33.
- Helwig, K., Poulin, J., Corbeil, M.-C., Moffatt, E., Duguay, D., 2014. Conservation issues in several twentieth-century Canadian oil paintings: The role of zinc carboxylate reaction products. In: van den Berg, K.J., Burnstock, A., de Keijzer, M., Krueger, J., Learner, T., de Tagle, A., Heydenreich, G. (Eds.), *Issues in Contemporary Oil Paint*. Springer, pp. 167–184.
- Henderson, E.J., Helwig, K., Read, S., Rosendahl, S.M., 2019. Infrared chemical mapping of degradation products in cross-sections from paintings and painted objects. *Herit. Sci.* 7 (71).
- Hermans, J.J., 2017. Metal soaps in oil paint – structure, mechanisms and dynamics. (Ph.D. thesis). University of Amsterdam.
- Hermans, J.J., Baij, L., Koenis, M., Keune, K., Iedema, P.D., Woutersen, S., 2019. 2D-IR spectroscopy for oil paint conservation: Elucidating the water-sensitive structure of zinc carboxylate clusters in ionomers. *Sci. Adv.* 5, eaaw3592.
- Hermans, J.J., Keune, K., van Loon, A., Corkery, R.W., Iedema, P.D., 2016a. Ionomer-like structure in mature oil paint binding media. *RSC Adv.* 6 (96), 93363–93369.
- Hermans, J.J., Keune, K., van Loon, A., Iedema, P.D., 2015. An infrared spectroscopic study of the nature of zinc carboxylates in oil paintings. *J. Anal. At. Spectrom.* 30 (7), 1600–1608.
- Hermans, J.J., Keune, K., van Loon, A., Iedema, P.D., 2016b. The crystallization of metal soaps and fatty acids in oil paint model systems. *Phys. Chem. Chem. Phys.* 18 (16), 10896–10905.
- Hermans, J.J., Osmond, G., van Loon, A., Iedema, P.D., Chapman, R., Drennan, J., Jack, K., Rasch, R., Morgan, G., Zhang, Z., Monteiro, M., Keune, K., 2018. Electron microscopy imaging of zinc soaps nucleation in oil paint. *Microsc. Microanal.* 24 (3), 318–322.
- Higgitt, C., Spring, M., Saunders, D., 2003. Pigment-medium interactions in oil paint films containing red lead or lead-tin yellow. *National Gallery Tech. Bull.* 24, 75–95.
- Hille, T.S., Nijdam, T.J., Suiker, A.S.J., Turteltaub, S., Sloof, W.G., 2009. Damage growth triggered by interface irregularities in thermal barrier coatings. *Acta Mater.* 57 (9), 2624–2630.
- Izzo, F.C., Kratter, M., Nevin, A., Zendri, E., 2021. A critical review on the analysis of metal soaps in oil paintings. *ChemistryOpen* 10 (9), 904–921.
- Keune, K., Boon, J.J., 2007. Analytical imaging studies of cross-sections of paintings affected by lead soap aggregate formation. *Stud. Conserv.* 52 (3), 161–176.
- Keune, K., Hoogland, F., Peggie, D., Higgitt, C., Boon, J.J., 2008. Comparative study of the effect of traditional pigments on artificially aged oil paint systems using complementary analytical techniques. In: Bridgland, J. (Ed.), *Diversity in Heritage Conservation: Tradition, Innovation and Participation*. Vol. II, New Delhi: Allied Publishers Pvt. Ltd., pp. 833–842, ICOM-CC 15th Triennial Conference Preprints, New Delhi, 22–26 September, 2008.
- Keune, K., Kramer, R.P., Huijbregts, Z., Schellen, H.L., Stappers, M.H.L., van Eikema Hommes, M.H., 2016. Pigment degradation in oil paint induced by indoor climate: Comparison of visual and computational backscattered electron images. *Microsc. Microanal.* 22 (2), 448–457.

- Keune, K., van Loon, A., Boon, J.J., 2011. SEM backscattered-electron images of paint cross sections as information source for the presence of the lead white pigment and lead-related degradation and migration phenomena in oil paintings. *Microsc. Microanal.* 17, 696–701.
- Lazzari, M., Chiantore, O., 1999. Drying and oxidative degradation of linseed oil. *Polym. Degrad. Stab.* 65 (2), 303–313.
- Lide, D.R. (Ed.), 2003. *CRC Handbook of Chemistry and Physics*, 84 CRC Press.
- Luimes, R.A., Suiker, A.S.J., 2021. Numerical modelling of climate-induced fracture and deformation in wood: Application to historical museum objects. *Int. J. Solids Struct.* 210–211, 237–254.
- Luimes, R.A., Suiker, A.S.J., Verhoosel, C.V., Jorissen, A.J.M., Schellen, H.L., 2018. Fracture behaviour of historic and new oak wood. *Wood Sci. Technol.* 52, 1243–1269.
- MacDonald, M.G., Palmer, M.R., Suchomel, M.R., Berrie, B.H., 2016. Reaction of Pb(II) and Zn(II) with ethyl linoleate to form structured hybrid inorganic-organic complexes: a model for degradation in historic paint films. *ACS Omega* 1 (3), 344–350.
- Maines, C.A., Rogala, D., Lake, S., Mecklenburg, M., 2011. Deterioration in abstract expressionist paintings: Analysis of zinc oxide paint layers in works from the collection of the Hirshhorn Museum and Sculpture Garden, Smithsonian Institute. 1319, 275–284.
- Martínez-Casado, F.J., Ramos-Riesco, M., Rodríguez-Cheda, J.A., Redondo-Yéamos, M.I., Garrido, L., Fernández-Martínez, A., García-Barriocanal, J., da Silva, I., Durán-Olivencia, M., Poulain, A., 2017. Lead(II) soaps: crystal structures, polymorphism, and solid and liquid mesophases. *Phys. Chem. Chem. Phys.* 19, 17009.
- Mecklenburg, M.F., Tumosa, C.S., Erhardt, D., 2004. The changing mechanical properties of aging oil paints. *MRS Proceedings* 852, OO3.1.
- Mecklenburg, M.F., Tumosa, C.S., Erhardt, D., 2012. The influence of pigments and ion migration on the durability of drying oil and alkyd paints. In: Mecklenburg, M.F., Charola, A.E., Koestler, R.J. (Eds.), *New Insights Into the Cleaning of Paintings*. Universidad Politécnica de Valencia, Smithsonian Contributions to Museum Conservation, pp. 59–67.
- Noble, P., 2019. A brief history of metal soaps in paintings from a conservation perspective. In: Casadio, F., Keune, K., Noble, P., van Loon, A., Hendriks, E., Centeno, S.A., Osmond, G. (Eds.), *Metal Soaps in Art: Conservation and Research*. Springer, pp. 1–22.
- Noble, P., Boon, J.J., 2007. Metal soap degradation of oil paintings: Aggregates, increased transparency and efflorescence. In: Parkin, H.M. (Ed.), *AIC Paintings Specialty Group Postprints: Papers Presented At the 34th Annual Meeting of the American Institute for Conservation of Historic & Artistic Works*, Providence, Rhode Island. Washington, D.C.: AIC, pp. 1–15.
- Noble, P., Boon, J.J., Wadum, J., 2002. Dissolution aggregation and protrusion: lead soap formation in 17th century grounds and paint layers. *ArtMatters* 1, 46–61.
- Ortiz Miranda, A.S., Kronkright, D., Walton, M., 2020. The influence of commercial primed canvases in the manifestation of metal soaps protrusions in Georgia O'Keeffe's oil paintings. *Herit. Sci.* 8 (107).
- Osmond, G., Boon, J.J., Puskar, L., Drennan, J., 2012. Metal stearate distributions in modern artists' oil paints: surface and cross-sectional investigation of reference paint films using conventional and synchrotron infrared microspectroscopy. *Appl. Spectrosc.* 66 (10), 1136–1144.
- Oxtoby, D.W., Gillis, H.P., Campion, A., 2008. *Principles of Modern Chemistry*, sixth ed. Thomson, Brooks/Cole, USA.
- Perles, A., Fuster-López, L., García-Diego, F.J., Peiró-Vitoria, A., García-Castillo, A.M., Andersen, C.K., Bosco, E., Mavrikas, E., Pariente, T., 2020. CollectionCare: an affordable service for the preventive conservation monitoring of single cultural artefacts during display, storage, handling and transport. *IOP Conf. Series: Mater. Sci. Eng.* 949, 012026.
- Plater, M.J., De Silva, B., Gelbrich, T., Hursthouse, M.B., Higgitt, C.L., Saunders, D.R., 2003. The characterisation of lead fatty acid soaps in 'protrusions' in aged traditional oil paint. *Polyhedron* 22, 3171–3179.
- Raven, L.E., Bisschoff, M., Leeuwestein, M., Geldof, M., Hermans, J.J., Stols-Witlox, M., Keune, K., 2019. Delamination due to zinc soap formation in an oil painting by Piet Mondrian (1872-1944). In: Casadio, F., Keune, K., Noble, P., van Loon, A., Hendriks, E., Centeno, S.A., Osmond, G. (Eds.), *Metal Soaps in Art: Conservation and Research*. Springer, pp. 343–358.
- Salvant, J., Barthel, E., Menu, M., 2011. Nanoindentation and the micromechanics of Van Gogh oil paints. *Appl. Phys. A* 104, 509–515.
- Schellekens, J.C.J., de Borst, R., 1993. On the numerical integration of interface elements. *Internat. J. Numer. Methods Engrg.* 36 (1), 43–66.
- Scheperboer, I.C., Luimes, R.A., Suiker, A.S.J., Bosco, E., Clemens, F.H.L.R., 2021. Experimental-numerical study on the structural failure of concrete sewer pipes. *Tunn. Undergr. Space Technol.* 116, 104075.
- Scheperboer, I.C., Suiker, A.S.J., Luimes, R.A., Bosco, E., Jorissen, A.J.M., 2019. Collapse response of two-dimensional cellular solids by plasticity and cracking – application to wood. *Int. J. Fract.* 219 (2), 221–244.
- Thoury, M., van Loon, A., Keune, K., Hermans, J.J., Réfrégiers, M., Berrie, B.H., 2019. Photoluminescence micro-imaging sheds new light on the development of metal soaps in oil paintings. In: Casadio, F., Keune, K., Noble, P., van Loon, A., Hendriks, E., Centeno, S.A., Osmond, G. (Eds.), *Metal Soaps in Art: Conservation and Research*. Springer, pp. 211–225.
- Tiennot, M., Paardekam, E., Iannuzzi, D., Hermens, E., 2020. Mapping the mechanical properties of paintings via nanoindentation: a new approach for cultural heritage studies. *Sci. Rep.* 10, 7924.
- Tijssens, M.G.A., van der Giessen, E., Sluys, L.J., 2000. Simulation of mode I crack growth in polymers by crazing. *Int. J. Solids Struct.* 37 (48–50), 7307–7327.
- Tudry, G.J., O'Reilly, M.V., Dou, S., King, D.R., Winey, K.I., Runt, J., Colby, R.H., 2012. Molecular mobility and cation conduction in polyether-ester-sulfonate copolymer ionomers. *Macromolecules* 45 (9), 3962–3973.
- van den Berg, J.D.J., 2002. *Analytical chemical studies on traditional oil paints* (Ph.D. thesis). University of Amsterdam.
- van den Berg, J.D.J., van den Berg, K.J., Boon, J.J., 2001. Determination of the degree of hydrolysis of oil paint samples using a two-step derivatisation method and on-column GC/MS. *Prog. Org. Coat.* 41 (1), 143–155.
- van der Weerd, J., Boon, J.J., Geldof, M., Heeren, R.M.A., Noble, P., 2002. Chemical changes in old master paintings: dissolution, metal soap formation and remineralisation processes in lead pigmented paint layers of 17th century paintings. *Zeitschrift FÜR Kunsttechnologie Und Konservierung* 16 (1), 36–51.
- van Gorkum, R., Bouwman, E., 2005. The oxidative drying of alkyd paint catalysed by metal complexes. *Coord. Chem. Rev.* 249, 1709–1728.
- van Loon, A., 2009. *De korrelige verf in Vermeers Gezicht op Delft*. Nieuwe onderzoeksgegevens. KM Materiaaltechnische Informatie over Kunst En Vormgeving 72, 10–13.
- van Loon, A., Noble, P., Burnstock, A., 2012. Ageing and deterioration of traditional oil and tempera paints. In: Stoner, J.H., Rushfield, R. (Eds.), *Conservation of Easel Paintings: Principle and Practice*. Butterworth-Heinemann, pp. 214–241.
- Xu, X.-P., Needleman, A., 1994. Numerical simulations of fast crack growth in brittle solids. *J. Mech. Phys. Solids* 42 (9), 1397–1434.
- Zumdahl, S.S., Zumdahl, S.A., 2017. *Chemistry*, ninth ed. Brooks/Cole Cengage Learning, USA.